



## SMA OBSERVATIONS OF THE EXTENDED $^{12}\text{CO}(J=6-5)$ EMISSION IN THE STARBURST GALAXY NGC 253

M. KRIPS<sup>1</sup>, S. MARTÍN<sup>1,2</sup>, A. B. PECK<sup>3</sup>, K. SAKAMOTO<sup>4</sup>, R. NERI<sup>1</sup>, M. GURWELL<sup>5</sup>, G. PETITPAS<sup>5</sup>, AND JUN-HUI ZHAO<sup>5</sup>

<sup>1</sup> Institut de RadioAstronomie Millimétrique, 300 rue de la Piscine, Domaine Universitaire,  
F-38406 Saint Martin d'Hères, France; krips@iram.fr, smartin@iram.fr, neri@iram.fr

<sup>2</sup> European Southern Observatory, Avda Alonso de Córdova 3107, Vitacura, Santiago, Chile

<sup>3</sup> National Radio Astronomy Observatory, 520 Edgemont Rd, Charlottesville, VA 22903, USA; apeck@nrao.edu

<sup>4</sup> Academia Sinica, Institute of Astronomy and Astrophysics, Taiwan; ksakamoto@asiaa.sinica.edu.tw

<sup>5</sup> Harvard-Smithsonian Center for Astrophysics, Cambridge, MA 02138, USA; mgurwell@cfa.harvard.edu,  
gpetipa@cfa.harvard.edu, jzhao@cfa.harvard.edu

Received 2014 June 30; accepted 2016 January 15; published 2016 April 20

### ABSTRACT

We present observations of the  $^{12}\text{CO}(J=6-5)$  line and 686 GHz continuum emission in NGC 253 with the Submillimeter Array at an angular resolution of  $\sim 4''$ . The  $^{12}\text{CO}(J=6-5)$  emission is clearly detected along the disk and follows the distribution of the lower  $^{12}\text{CO}$  line transitions with little variation of the line ratios. A large velocity gradient analysis suggests a two-temperature model of the molecular gas in the disk, likely dominated by a combination of low-velocity shocks and the disk-wide photodissociation regions. Only marginal  $^{12}\text{CO}(J=6-5)$  emission is detected in the vicinity of the expanding shells at the eastern and western edges of the disk. While the eastern shell contains gas even warmer ( $T_{\text{kin}} > 300$  K) than the hot gas component ( $T_{\text{kin}} = 300$  K) of the disk, the western shell is surrounded by gas much cooler ( $T_{\text{kin}} = 60$  K) than the eastern shell but somewhat hotter than the cold gas component of the disk (for similar H<sub>2</sub> and CO column densities), indicative of different (or differently efficient) heating mechanisms. The continuum emission at 686 GHz in the disk agrees well in shape and size with that at lower (sub)millimeter frequencies, exhibiting a spectral index consistent with thermal dust emission. We find dust temperatures of  $\sim 10$ –30 K and largely optically thin emission. However, our fits suggest a second (more optically thick) dust component at higher temperatures ( $T_{\text{d}} > 60$  K), similar to the molecular gas. We estimate a global dust mass of  $\sim 10^6 M_{\odot}$  for the disk, translating into a gas-to-dust mass ratio of a few hundred, consistent with other nearby active galaxies.

**Key words:** galaxies: active – galaxies: individual (NGC 253) – galaxies: ISM – galaxies: starburst – ISM: molecules – submillimeter: galaxies

### 1. INTRODUCTION

Submillimeter interferometric observations at frequencies above 400 GHz are technically difficult and rely on very dry atmospheric conditions. The reduced transmissivity of the atmosphere at submillimeter wavelengths necessitates observing from a vantage point at high elevation ( $\gtrsim 4000$  m above sea level). Before the advent of the Atacama Large Millimeter Array (ALMA), the only interferometer in the world offering the capability of observations at frequencies above 400 GHz was the Submillimeter Array (SMA), located at 4000 m altitude on Mauna Kea in Hawaii, USA. Equipped with eight antennas of 6 m diameter and 690 GHz receivers, the SMA provides a window on warm and hot molecular gas and dust through the  $^{12}\text{CO}(J=6-5)$  line and submillimeter continuum emission with high angular resolution. The analysis of spatially resolved warm molecular gas provides essential information to understand the complexity of the excitation conditions, chemistry and dynamics of the molecular gas in various environments, including star-forming regions, active galactic nuclei (AGNs) and quiescent regions (e.g., Martín et al. 2006; Aladro et al. 2011; Krips et al. 2008, 2011). Moreover, given the explosion of detections of molecular gas at high redshifts in the past decade, mostly through high rotational levels of CO, it is essential to have a robust understanding of the physics behind the CO ladder as a function of the energetic environments in which they are detected (e.g., Carilli et al. 2002; Weiß et al. 2005; Papadopoulos et al. 2007, 2010; Rosenberg et al. 2014). To date, only a handful of journal

publications exist based on 690 GHz interferometric observations, most of which study Galactic sources (e.g., Beuther et al. 2006; Qi et al. 2006; Nakashima et al. 2007; Matsushita et al. 2009; Roloffs et al. 2011; Zapata et al. 2013). Matsushita et al. (2009) present the first 690 GHz interferometric study of  $^{12}\text{CO}$  ( $J=6-5$ ) emission in a nearby extragalactic source, the ultraluminous infrared galaxy Arp 220. Since then, mostly thanks to ALMA but also the SMA, a couple of interferometric observations of the  $^{12}\text{CO}(J=6-5)$  emission in nearby galaxies have been published recently (e.g., Sliwa et al. 2013; García-Burillo et al. 2014; Xu et al. 2014). In this paper, we present the first mosaic observations at 690 GHz of the nearby starburst galaxy NGC 253, made using the SMA.

NGC 253 is one of the best studied nearby ( $\sim 3.5$  Mpc, where  $1'' = 17$  pc; Mouhcine et al. 2005; Rekola et al. 2005) infrared bright starburst galaxies ( $3 \times 10^{10} L_{\odot}$ ; Telesco & Harper 1980). It is thus an ideal prototype to study the effects of a central starburst ( $\sim 2$ –4  $M_{\odot}$  yr $^{-1}$ ; Ott et al. 2005; Minh et al. 2007; Bendo et al. 2015) on the dynamics (NGC 253 is an edge-on galaxy), excitation conditions, and chemistry of the surrounding molecular gas (e.g., Bradford et al. 2003; Martín et al. 2006; Sakamoto et al. 2006, 2011; Knudsen et al. 2007; Bolatto et al. 2013; Leroy et al. 2015; Meier 2015). As a consequence of the starburst in the center of NGC 253, a high rate of supernova explosions ( $< 0.2$  yr $^{-1}$ ) has been observed (see Paglione & Abrahams 2012; Rampadarath et al. 2014). These are most likely responsible for a kiloparsec-scale outflow perpendicular to the disk (e.g., Fabbiano & Trinchieri 1984;

Heckman et al. 1990). In addition to this outflow, Sakamoto et al. (2006) report on at least two expanding shells, or superbubbles, at the edges of the disk (named SB1 for the south-western shell and SB2 for the north-eastern one), which might be caused by either winds from and/or supernovae in a super star cluster or a hypernova(e); the possibility of a third shell, a bit further south than SB2, was discussed as well. The authors further find a strongly disturbed molecular gas disk associated with young stellar clusters and stellar explosions as well as the large-scale super-wind. Their follow-up observations at  $\sim 1''$  resolutions confirmed the SB2 (and the third shell) but SB1 was reported to be more complicated than it appeared in previous lower-resolution data (Sakamoto et al. 2011). They noted that it may be a shell in a complicated shape or other gas kinematic feature that looks like a shell at low resolution. With very recent ALMA observations of  $^{12}\text{CO}(J=1-0)$  at  $3''$  resolution Bolatto et al. (2013) reported four shells in the central kiloparsec of NGC 253. One is SB2 and three are clustered in/around the region of SB1. While SB2 can be connected to a compact stellar cluster, SB1 is found at the position of a compact radio continuum source that is associated with a supernova remnant (see Sakamoto et al. 2006; Bolatto et al. 2013). The nature of shells 2 and 4 remains unclear at this point, whether they are separate bubbles or connected to the stellar winds or other dynamical features.

A 2 mm line survey of NGC 253 done by Martín et al. (2006) reveals an impressive chemical richness and complexity in its center (see also Meier 2015). NGC 253 appears to resemble SgrB2, the region of molecular cloud complexes in the Galactic center, more than the evolved starburst galaxy M82 (see also Aladro et al. 2011) despite the fact that our Milky Way is not a starburst galaxy at all. Moreover, Sakamoto et al. (2011) find a striking resemblance between the molecular gas distribution of the Milky Way and that of NGC 253. The chemistry of the molecular gas in the central kiloparsec of NGC 253 appears to be dominated by large-scale, low-velocity shocks (e.g., García-Burillo et al. 2000; Martín et al. 2006). However, Martín et al. (2009) detect significant amounts of molecular tracers for photodissociation regions (PDRs), suggesting that PDR chemistry also plays a significant role in this starburst galaxy. This is further supported by Rosenberg et al. (2012, 2014). The NIR H<sub>2</sub> emission appears to be mostly fluorescently excited, favoring PDRs as the dominant excitation mechanism in the nuclear region of NGC 253. The only exceptions seem to be three small isolated regions in which shocks may play the leading role. Rosenberg et al. (2012) estimate that at most 30% of the H<sub>2</sub> emission is excited by shocks. Based on a ladder analysis of  $^{12}\text{CO}$  and  $^{13}\text{CO}$  from *Herschel* and ground-based single-dish observations with a (normalized) beam of  $32''.5$ , Rosenberg et al. (2014) present even more evidence for the combined contribution of PDR and mechanical heating of the molecular gas in the central disk of NGC 253. They also argue that heating by cosmic rays can mostly be neglected; at most a few percent could be attributed to cosmic-ray heating in their models.

The paper is organized as follows. The observations and the archival data are discussed in Section 2. The results are discussed in Section 3 and a summary is given in Section 4.

## 2. OBSERVATIONS

First, we will present some general information on the SMA observations conducted for this paper. We will then briefly

discuss previous  $^{12}\text{CO}(J=3-2)$  SMA observations that were eventually used to merge with the  $^{12}\text{CO}(J=3-2)$  observations carried out simultaneously with  $^{12}\text{CO}(J=6-5)$ . We will give additional information on previous  $^{12}\text{CO}(J=2-1)$  SMA observations. These observations were taken from Sakamoto et al. (2006, 2011). New  $^{12}\text{CO}(J=1-0)$  ALMA observations of NGC 253 are also included in this study and are hence briefly presented as well. We will address the problem of missing short spacings and the significance of spatial filtering to our observations in Section 2.4. All data presented in this paper stem from mosaic observations (except the  $^{12}\text{CO}(J=2-1)$  data) and have hence been corrected for the respective primary beams.

### 2.1. SMA Observations of $^{12}\text{CO}(J=6-5)$ and $^{12}\text{CO}(J=3-2)$

NGC 253 was observed using two receivers simultaneously to obtain  $^{12}\text{CO}(J=6-5)$ ,  $^{12}\text{CO}(J=3-2)$ , and  $\text{HCO}^+(J=4-3)$ <sup>6</sup> with the SMA. At the time of the observations, five of the eight SMA antennas were equipped with working 690 GHz receivers. All five antennas were placed in the inner ring of the array, known as the sub-compact configuration, with baselines ranging from a few meters ( $\sim 8$  m) up to 25 m to allow for a good ( $u$ ,  $v$ ) coverage and reasonable angular resolution at 690 GHz. To cover most of the CO emission in NGC 253, a five-field mosaic (size  $\simeq 50''$ ) along the plane of the disk was observed with a spacing of half the primary beam size ( $\sim 7.5''$ ) at 690 GHz between the pointing centers. The phase reference center of the central pointing was set to  $\alpha(J2000) = 00^{\text{h}}47^{\text{m}}33.241$  and  $\delta(J2000) = -25^{\circ}17'18.16$ . Considering the small primary beam of  $\sim 15''$  at 690 GHz and thus the increased need for accurate pointing, regular pointing offset updates (i.e., every  $\sim 3$  hr) were conducted on either 3C454.3 or 3C111 (using interferometry) or Jupiter (using single-dish measurements) throughout the night at 345 GHz. All spectral windows covered 2 GHz in bandwidth, and the lower sideband (LSB) of the lower frequency was tuned to the  $^{12}\text{CO}(J=3-2)$  line so that the  $\text{HCO}^+(J=4-3)$  line fell into the corresponding upper sideband (USB), situated 10 GHz above the LSB. The USB of the 690 GHz receivers was tuned to the  $^{12}\text{CO}(J=6-5)$  line, leaving the corresponding LSB for continuum measurements. The weather was excellent, with a 225 GHz atmospheric opacity of  $\sim 0.05\text{--}0.1$  throughout the track. This corresponds to single-sideband (SSB) system temperatures of  $T_{\text{sys}}(\text{SSB}) = 5000\text{--}10,000$  K at 690 GHz and  $T_{\text{sys}}(\text{SSB}) = 400\text{--}800$  K at 345 GHz. We used the nearby ( $\sim 20^\circ$  from NGC 253) planet Uranus as calibrator for bandpass, gain, and absolute flux. The calibration on Uranus was performed using a disk model to compensate for the fact that it was slightly resolved. The quality of the gain calibration was verified against a nearby quasar (J2348-1631), which was observed with the same cycle times as Uranus. It appears to be of symmetric Gaussian shape at both frequencies but slightly shifted ( $\sim +0.8''$ ) in declination from its phase center at 690 GHz while being centered correctly at 345 GHz after applying the gain calibration. The spatial shift at 690 GHz indicates a problem with the phase transfer at 690 GHz, probably due to uncertainties in the measured baseline and/or larger distance of NGC 253 from the phase calibrator; the baseline error is around  $0.3\lambda$  at 690 GHz. We hence consider

<sup>6</sup> Further analysis of the  $\text{HCO}^+(J=4-3)$  data may be presented separately, while this paper is concerned with only the  $^{12}\text{CO}$  transitions.

**Table 1**  
Observation Log

Line	Frequency (GHz)	Date	rms <sup>a</sup> (mJy)	$\Delta v$ (km s $^{-1}$ )	Beam <sup>b</sup>	Type <sup>c</sup>	References <sup>d</sup>
$^{12}\text{CO}(J = 6-5)$	691.473 (USB)	2007 Sep	7000	12	$4.^{\prime\prime}2 \times 2.^{\prime\prime}1$	M	(1)
$^{12}\text{CO}(J = 3-2)e$	345.796 (LSB)	2007 Sep	100	12	$5.^{\prime\prime}8 \times 4.^{\prime\prime}5$	M	(1)
$^{12}\text{CO}(J = 3-2)e$	345.796 (LSB)	2004 Sep	130	12	$3.^{\prime\prime}9 \times 1.^{\prime\prime}9$	M	(2)
$^{12}\text{CO}(J = 2-1)f$	230.538 (LSB,USB)	2003–2005	30	12	$1.^{\prime\prime}7 \times 1.^{\prime\prime}5$	SF	(2)
$^{12}\text{CO}(J = 1-0)$	115.271 (USB)	2011	4	12	$3.^{\prime\prime}7 \times 2.^{\prime\prime}7$	M	(3)

#### Notes.

<sup>a</sup> The noise given here corresponds to the thermal noise, as derived from the visibility weights, i.e., system temperatures. The noise is given per individual mosaic field (see the text for some more discussion).

<sup>b</sup> “Original” synthesized resolution for natural weighting. Note that all maps presented in this paper were brought to the same resolution of  $4.^{\prime\prime}2 \times 2.^{\prime\prime}1$  using a uv-taper to change the weighting for the different baselines.

<sup>c</sup> M = Mosaic; SF = Single Field

<sup>d</sup> (1) This work, (2) Sakamoto et al. (2011), (3) ALMA science archive; project id: 2011.0.00172.S.

<sup>e</sup> These two data sets were eventually combined (see text).

<sup>f</sup> These data were taken using all available configurations of the SMA, with baselines ranging from 8 to 509 m, as well being observed in different sidebands.

this effect as a systematic instrumental and calibrational artifact and correct the data for this  $\sim 0.^{\prime\prime}8$  shift. A similar positional shift was found for the 690 GHz SMA observations of Arp 220, which was also attributed to baseline errors by Matsushita et al. (2009). The accuracy of the flux calibration is estimated to be within 30% at 690 GHz and  $\sim 20\%$  at 345 GHz.

Angular resolutions of  $4.^{\prime\prime}2 \times 2.^{\prime\prime}1$  at position angle PA =  $162^{\circ}$  are obtained at 690 GHz and of  $5.^{\prime\prime}8 \times 4.^{\prime\prime}2$  at PA =  $173^{\circ}$  at 345 GHz. We reach an rms noise level of  $1\sigma = 100 \text{ mJy beam}^{-1} \text{ channel}^{-1}$  at 345 GHz and of  $1\sigma = 7 \text{ Jy beam}^{-1} \text{ channel}^{-1}$  at 691 GHz per individual mosaic field and for a spectral resolution of  $12 \text{ km s}^{-1}$ . Note that we used a Nyquist sampling to place the mosaic fields based on the 690 GHz field of view so that in the combined mosaic maps at 690 GHz the noise distribution is not homogeneous and will increase toward the edges and be a factor of  $\sqrt{2}$  smaller in the overlap regions; the mosaic fields at 345 GHz will, however, overlap by a much larger fraction so that the noise distribution is much more homogeneous there. The latter fact has been taken into account in our estimate of the  $1\sigma$  levels for each figure (see their captions). A log of the observations is given in Table 1.

We subtracted the strong continuum emission found in NGC 253, averaged over all line-free channels in each sideband, from the original data cubes to generate pure line emission data.

## 2.2. Previous SMA Observations of $^{12}\text{CO}(J = 3-2)$ and $^{12}\text{CO}(J = 2-1)$

In order to enable a direct comparison between the  $^{12}\text{CO}(J = 6-5)$  emission and the lower- $J$  CO emission and reduce systematic biases such as resolution effects due to different synthesized beams and uv-coverages, we merged our  $^{12}\text{CO}(J = 3-2)$  data with the high-spectral-resolution data at 345 GHz presented by Sakamoto et al. (2011). In the merged  $^{12}\text{CO}(J = 3-2)$  data set we then reach an rms noise level of  $1\sigma = 80 \text{ mJy beam}^{-1} \text{ channel}^{-1}$  per mosaic field or  $\sim 60 \text{ mJy beam}^{-1} \text{ channel}^{-1}$  in the center of the mosaic for a spectral resolution of  $12 \text{ km s}^{-1}$ . We also included the  $^{12}\text{CO}(J = 2-1)$  data of Sakamoto et al. (2006, 2011), which are already a combination of observations with low and high

spatial resolution; the rms is found to be  $25 \text{ mJy beam}^{-1} \text{ channel}^{-1}$  (using only a single field) at a spectral resolution of  $12 \text{ km s}^{-1}$ . In order to match the resolution of  $^{12}\text{CO}(J = 3-2)$  and  $^{12}\text{CO}(J = 2-1)$  to that of  $^{12}\text{CO}(J = 6-5)$ , we used a uv-taper, obtaining an angular resolution of  $4.^{\prime\prime}2 \times 2.^{\prime\prime}1$ . We did not find significant differences with this method compared to matching the uv-coverages of the  $^{12}\text{CO}(J = 3-2)$  and  $^{12}\text{CO}(J = 2-1)$  data to that of  $^{12}\text{CO}(J = 6-5)$ . In order to preserve the data in their entirety, we hence chose the first method.

## 2.3. ALMA Observations of $^{12}\text{CO}(J = 1-0)$

ALMA cycle 0 observations are available for the  $^{12}\text{CO}(J = 1-0)$  line from the ALMA science archive, which were made in the compact configuration with up to 19 antennas (project id: 2011.0.00172.S; see also Bolatto et al. 2013). The  $^{12}\text{CO}(J = 1-0)$  line was tuned to the USB within a 2 GHz wide spectral window using a spectral resolution of 488 kHz ( $\simeq 1.3 \text{ km s}^{-1}$ ). Uranus was used as an absolute flux calibrator, J2333-237 as a bandpass calibrator, and J0137-245 as phase and amplitude calibrator. Using the strong continuum emission, self-calibration was applied to the phases to improve the image quality of the continuum and line maps. Given the excellent uv-coverage, we used a slight uv-taper to smooth the initial spatial resolution to the angular resolution of our  $^{12}\text{CO}(J = 6-5)$  observations. Data reduction was done using CASA but further image processing was done in GILDAS. As with the other datasets, the continuum was derived from the line-free channels and then subsequently subtracted from the channels containing both line and continuum emission.

## 2.4. Effects of Spatial Filtering

In order to assess the lack of short spacings and hence missing flux, we have compared our observations with existing single-dish observations. Bayet et al. (2004) have observed the  $^{12}\text{CO}(J = 6-5)$  emission in NGC 253 using the Caltech Submillimeter Observatory (CSO). In the central  $10.^{\prime\prime}5$ , they obtain an integrated intensity of  $1394 \pm 279 \text{ K km s}^{-1}$ , which

<sup>7</sup> That is, restricting the uv-coverages to the overlapping regions.

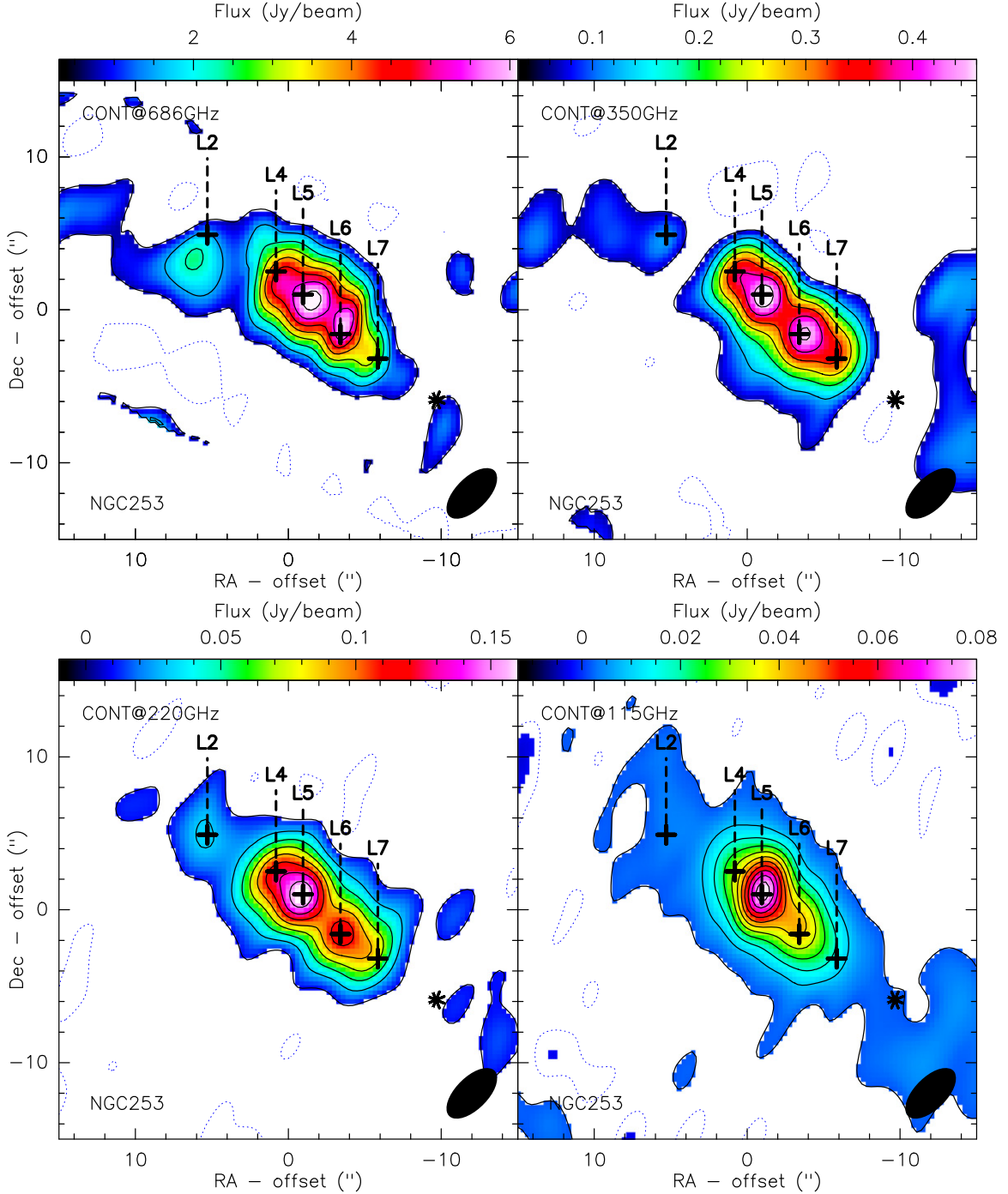


**Figure 1.** Continuum emission at 686 GHz (upper left), 350 GHz (upper right), 220 GHz (lower left), and 115 GHz (lower right), all at a spatial resolution of  $\sim 4''.2 \times 2''.1$ . The contours of the 686 GHz continuum emission start at  $-2\sigma$ ,  $2\sigma = 0.76 \text{ Jy beam}^{-1}$  in steps of  $2\sigma$ , those of the 350 GHz continuum emission start at  $-5\sigma$ ,  $10\sigma = 0.064 \text{ Jy beam}^{-1}$  and go then in steps of  $10\sigma$ , those of the 220 GHz continuum emission start at  $-3\sigma$ ,  $5\sigma = 0.01 \text{ Jy beam}^{-1}$  and go in steps of  $10\sigma$ , and those of the 115 GHz continuum emission start at  $-10\sigma$ ,  $10\sigma = 1.5 \text{ mJy beam}^{-1}$  and go in steps of  $50\sigma$ . The black crosses indicated in each panel mark the positions of the respective line emission peaks defined in Figure 4 that match those of the continuum peaks shown here and are in good agreement with the 1.3 mm continuum emission peaks from Sakamoto et al. (2011). The black star marks the position of the western superbubble/shell from Sakamoto et al. (2006). Note that the eastern superbubble/shell lies outside the maps and is not shown here since no continuum emission is detected around it. The ( $0'', 0''$ ) offset is relative to the following absolute position:  $\alpha(J2000) = 00^{\text{h}}47^{\text{m}}33\overset{\text{s}}{.}241$  and  $\delta(J2000) = -25^{\circ}17'18\overset{\text{s}}{.}16$ .

corresponds to  $\sim(55,000 \pm 11,000) \text{ Jy km s}^{-1}$  assuming a conversion factor of  $S/T_{\text{mb}} = 39 \text{ Jy K}^{-1}$ . The SMA observations yield an integrated line intensity of  $\sim 45,000 \text{ Jy km s}^{-1}$  in the central  $10''.5$ , a bit less than that from the single-dish observations but still within the large uncertainties ( $\sim 20\%$

30%) in both measurements. For the  $^{12}\text{CO}(J=3-2)$  line emission, we find integrated line intensities of  $\sim 45000 \text{ Jy km s}^{-1}$  in the central  $\sim 20''$ , very similar to those obtained from the single-dish measurements in the same area discussed in Bayet et al. (2004). Hence, the SMA observations

**Table 2**  
General Results

Line $^{12}\text{CO}$	$S_{\nu}^{\text{max,a}}$ (Jy)	$v_0^{\text{max,a}}$ (km s $^{-1}$ )	FWHM $^{\text{max,a}}$ (km s $^{-1}$ )	$\int (S_{\nu} dv)^b$ (Jy km s $^{-1}$ )
J = 6–5	$350 \pm 15$	$0 \pm 3$	$130 \pm 7$	$(58 \pm 3) \times 10^3$
J = 3–2	$347 \pm 3$	$0 \pm 1$	$140 \pm 7$	$(75 \pm 2) \times 10^3$
J = 2–1	$111 \pm 2$	$0 \pm 1$	$167 \pm 8$	$(29 \pm 0.3) \times 10^3$
J = 1–0	$30 \pm 1$	$0 \pm 1$	$165 \pm 8$	$(7.8 \pm 0.1) \times 10^3$
Continuum $\nu_{\text{obs}}$	$S_{\nu}^b$ (Jy)			
686 GHz	$32 \pm 1.4$			
350 GHz	$2.6 \pm 0.1$			
220 GHz	$0.67 \pm 0.05$			
115 GHz	$0.26 \pm 0.01$			

#### Notes.

<sup>a</sup> Peak fluxes, zero velocities, and FWHM are given for the dominant maximum component of the multiple Gaussian fit. The zero velocity is with respect to the redshifted frequency of the respective CO line. The redshift of NGC 253 is  $z = 0.000811$  (see Koribalski et al. 2004).

<sup>b</sup> Emission taken over the entire emission area covered with the five-point mosaic by using a multiple Gaussian fit (up to three Gaussian lines are fitted).

**Table 3**  
Peak Fluxes for the Individual Continuum Peaks

ID	686 GHz <sup>a</sup> (mJy beam $^{-1}$ )	350 GHz <sup>a</sup> (mJy beam $^{-1}$ )	220 GHz <sup>a</sup> (mJy beam $^{-1}$ )	115 GHz <sup>a</sup> (mJy beam $^{-1}$ )
L2	$1700 \pm 400$	$114 \pm 6$	$33 \pm 2$	$3 \pm 0.15$
L4	$4000 \pm 400$	$326 \pm 6$	$115 \pm 2$	$28 \pm 0.15$
L5	$5800 \pm 400$	$474 \pm 6$	$166 \pm 2$	$81 \pm 0.15$
L6	$5900 \pm 400$	$456 \pm 6$	$121 \pm 2$	$40 \pm 0.15$
L7	$2900 \pm 400$	$330 \pm 6$	$076 \pm 2$	$14 \pm 0.15$

#### Note.

<sup>a</sup> Errors are based on noise levels; a synthesized matched beam of  $4.^{\prime\prime}2 \times 2.^{\prime\prime}1$  is used for all frequencies.

did not resolve out significant emission from the  $^{12}\text{CO}(J=3–2)$  and  $^{12}\text{CO}(J=6–5)$  lines (at least within the central  $\sim 10.^{\prime\prime}–20.^{\prime\prime}$ ).<sup>8</sup>

The  $^{12}\text{CO}(J=1–0)$  was observed by Houghton et al. (1997) using the SEST telescope. They derive an integrated intensity of  $377 \text{ K km s}^{-1}$  in the central  $\sim 30.^{\prime\prime}$  of NGC 253. Using a conversion factor of  $S/T_{\text{mb}} = 19 \text{ Jy K}^{-1}$ , this translates into  $7100 \text{ Jy km s}^{-1}$ . We find  $\sim 7000 \text{ Jy km s}^{-1}$  in the central  $\sim 30.^{\prime\prime}$  as well, indicating that no flux has been resolved out with ALMA, at least in the center of NGC 253.

## 3. RESULTS AND DISCUSSION

### 3.1. Continuum Emission

In our new SMA observations, continuum emission has been detected at 345 GHz (LSB), 355 GHz (USB), 681 GHz (LSB), and 691 GHz (USB) and is consistent between the two sidebands, accounting for the frequency difference of 10 GHz

<sup>8</sup> Note that no single-dish observations exist to cover the entire area of the five-point mosaic observations conducted for this paper. The estimates of resolution effects are hence only for the central disk and do not cover the two outer shells.

between the sidebands. The upper left panel of Figure 1 shows the sideband-averaged continuum emission at 686 GHz, the upper right panel shows 350 GHz (merged with the data from Sakamoto et al. 2011), the lower left panel that of 220 GHz and the lower right panel that of 115 GHz. As mentioned before, all four continuum images were made with the same angular resolution. The distribution of the continuum emission is fairly similar among the four frequencies. The 686 GHz emission shows the same peaks as previously identified by Sakamoto et al. (2011) at higher angular resolution, marked with black crosses in Figure 1. We labelled them L2 to L7 in this paper to facilitate a comparison with the line emission because the continuum peaks agree well in position with the corresponding line peaks (see definitions in Figure 4). L5 and L6 appear to be slightly closer together at 686 GHz than at the lower frequencies and L2 is somewhat offset in declination, i.e.,  $\sim 2.^{\prime\prime}$  ( $\simeq$ half the synthesized beam), at 686 GHz with respect to the lower frequencies. This discrepancy is larger than the uncertainties in the absolute and relative positions of the peaks and might suggest a region of warmer dust close to L2. Indeed, Bradford et al. (2003) identified an overabundance of  $^{12}\text{CO}$  ( $J=7–6$ ) in the same region as well. The brightnesses of the different peaks and their respective ratios to each other are very similar along the five continuum peaks, with L5 being the strongest, followed by L6, L4, L7, and L2.

Table 2 lists the total continuum fluxes for all four frequencies and Table 3 the individual fluxes per beam for each continuum peak. Assuming no significant resolution effects, the different fluxes indicate a total spectral index of +3 (for  $S_{\nu} \propto \nu^{\alpha}$ ), see also Figure 2. This is consistent with the spectral index found between the 1.3 mm and 0.87 mm continuum emission by Sakamoto et al. (2011) and between the 2.6 and 1.3 mm continuum by Sakamoto et al. (2006). This strongly indicates that the emission at  $>115$  GHz is largely dominated by thermal dust emission. Our new 690 GHz data, along with the ALMA 115 GHz data, now reveal differences in continuum intensity ratios among the continuum peaks (see Figures 2 and 3); Figure 2 shows the maps of spectral emissivity index between the different frequencies and Figure 3 plots the continuum spectral energy distribution (SED) for each of the continuum peaks normalized to the peak flux at 220 GHz for each component. While it is true that along L4–L7 the ratios do not change too much, yielding still an index around 3, it increases to  $\sim 4–5$  at L2 at least for the higher frequencies (see Figure 2). This appears to be consistent with the overabundance of  $^{12}\text{CO}(J=7–6)$  found by Bradford et al. (2003), suggesting a warmer dust component in this region. The latter would add to a higher flux of the 690 GHz continuum emission assuming a two-temperature phase of the dust here. Also, we see a slight drop in the spectral index with respect to the 2.6 mm continuum, which most likely indicates the increasing role of non-thermal synchrotron and thermal free-free continuum emission toward longer wavelengths (see Figure 3); Heesen et al. (2011) and Ulvestad & Antonucci (1997) find a probably equal contribution between non-thermal synchrotron radio emission presumably from supernova remnants and thermal free-free radio emission from H II regions, i.e., star formation. Heesen et al. (2011) derive a spectral index of  $\sim -0.5$  for the radio continuum emission at centimeter wavelengths in the center, which steepens to  $-2$  toward the outer parts and filaments. Judging from Figure 9 in Heesen et al. (2011), L5 and L6 show a spectral index of around  $-0.5$ , while L2, L4,

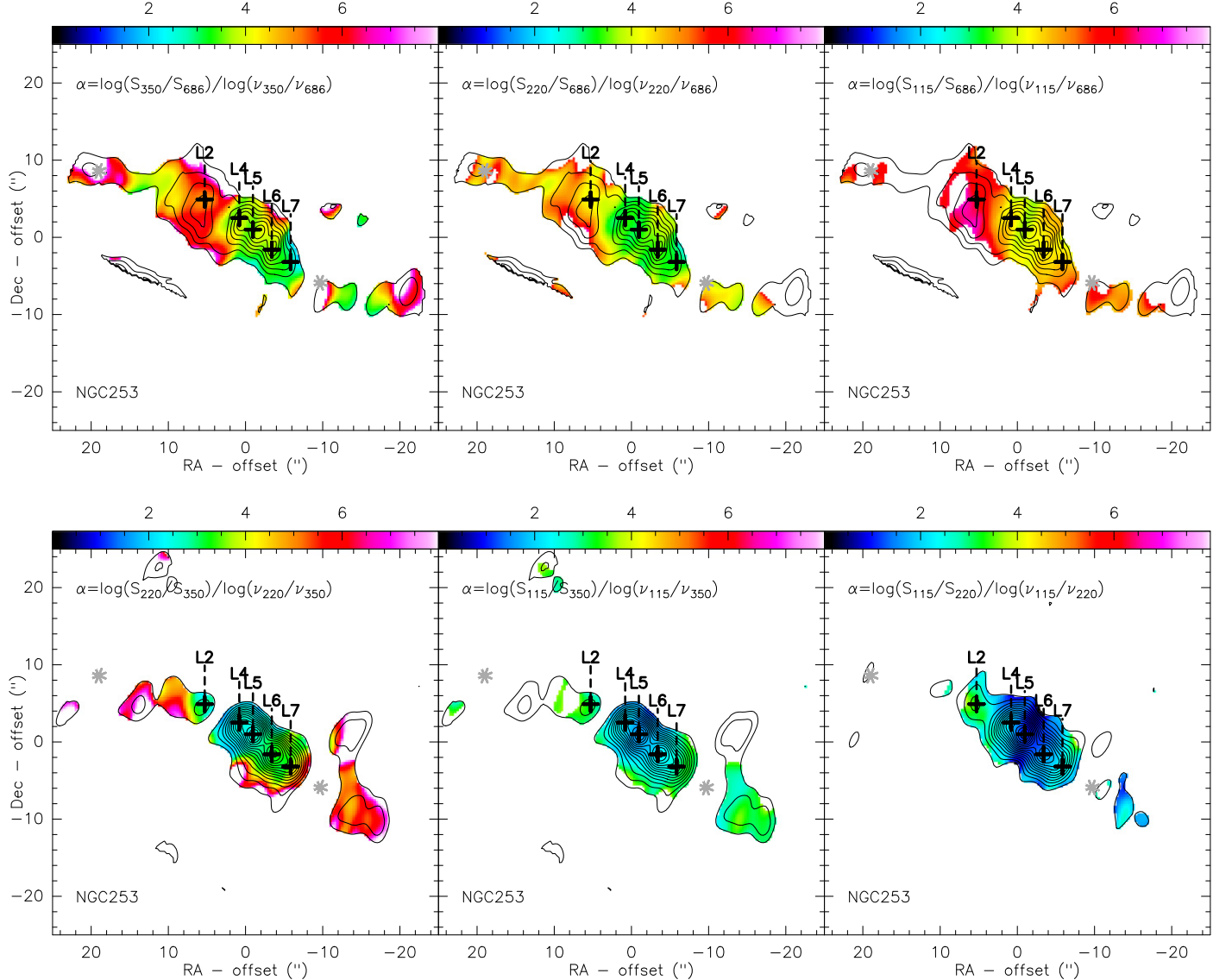


**Figure 2.** Spectral emissivity indices (labeled  $\alpha$  in the images) derived from the continuum emission at 686, 350, 220, and 115 GHz. The contours are the same as in Figure 1 and are from the continuum emission at the frequency in the respective denominator. The gray stars and black crosses are the same as in Figure 1.

and L7 increase to around  $-1$ , explaining the differences in the deviations of the 115 GHz continuum from the thermal (sub) millimeter (modified blackbody) slope for the different components. Depending on the component and assumed spectral index, the synchrotron/free-free emission contributes between 15% and 80% to the 115 GHz continuum emission, with L2 having the smallest (15%) and L5 and L7 ( $\sim 80\%$ ) having the largest contribution from these radio (centimeter/millimeter) processes to their 2.6 mm continuum emission. However, if the synchrotron/free-free spectral indices are somewhat flatter or steeper, the fraction of the total continuum emission contributed by this emission will change accordingly (being higher or lower, respectively). Given that generally (but not exclusively) the radio spectrum of non-thermal synchrotron continuum emission is steeper (i.e.,  $\alpha \simeq -0.5$  to  $-1$ ) than that of the thermal free-free continuum emission, it might be likely that the continuum emission at 2.6 mm has a larger contribution of thermal free-free emission (see also Peel et al. 2011). However, this might change from clump to clump within the

disk and we have no actual way to distinguish between non-thermal synchrotron and thermal free-free emission from our continuum observations other than the spectral radio index (which might be misleading). Therefore, we will not further stress a differentiation between the two processes.

### 3.1.1. Temperature, Opacity, and Mass of the Dust

While fitting a simple power law to the (sub)millimeter dust emission is a reasonable first-order approach, we can actually do better and determine the temperature, opacity, and dust mass from our observations, using standard equations (for a comparison on similar observations and sources see also the recent work on 690 GHz ALMA data for Arp 220 by Wilson et al. 2014; Scoville et al. 2015). By using flux ratios, we can eliminate some assumptions such as on the dust emissivity, in particular to derive the dust opacities and dust temperatures (but see also further below for the dust mass, for which this approach does not work). This gives the following

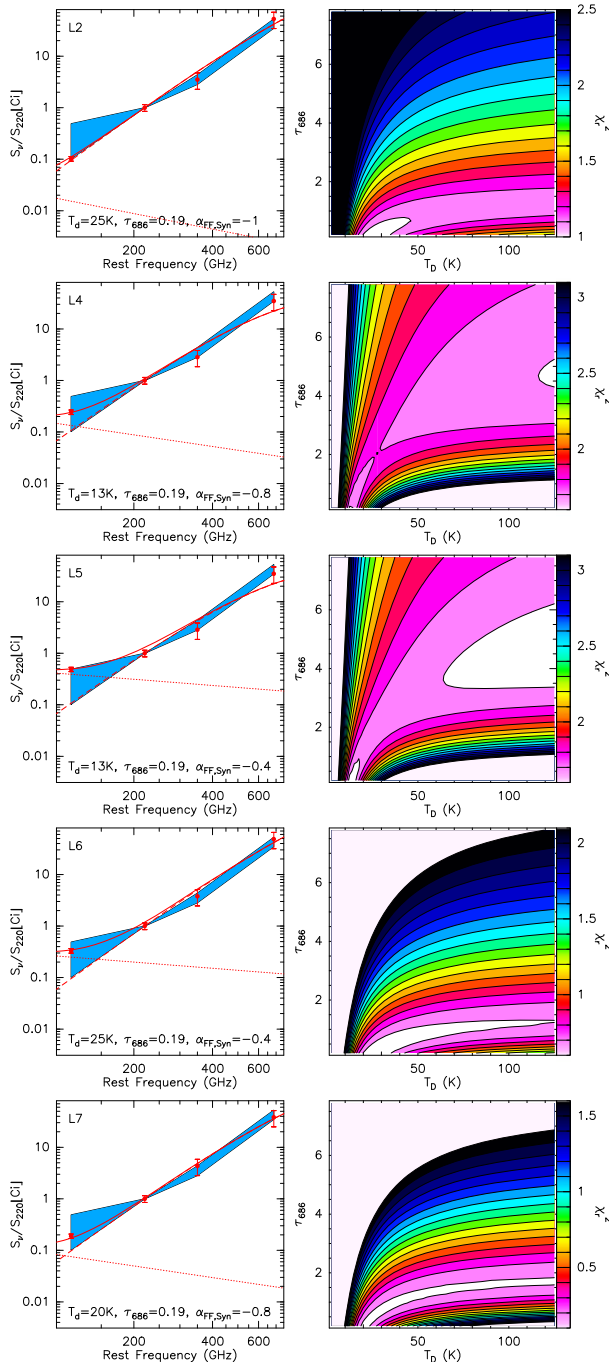


**Figure 3.** Continuum SED for the different continuum peaks (only peak fluxes taken for each frequency; left panel), normalized to the respective continuum fluxes at 230 GHz for each component (note the logarithmic scale of the flux ratio) and the corresponding best-fit solution (i.e., lowest reduced  $\chi^2_r$ , right panel) for each continuum peak assuming a dust emissivity of  $\beta = 1.8$  (see text for more details). The dashed and dotted lines represent the thermal (from a modified blackbody) and non-thermal synchrotron plus thermal free-free contribution to the emission, while the solid line is the composite of both. The dashed line has been fitted to the data, while the dotted line was made using a fixed beta of 1.8 from Heesen et al. (2011) (there are not enough observational data to conduct a thorough fit for beta as well). The error bars correspond to  $\pm 1\sigma$ . The blue shaded areas plotted in each panel on the left indicate the range of continuum fluxes found at the positions of L2–L7, i.e., they correspond to  $\text{min}(\text{flux} @ (\text{L2} \text{--} \text{L7}))$  to  $\text{max}(\text{flux} @ (\text{L2} \text{--} \text{L7}))$  at each wavelength.  $T_d$  is the dust temperature,  $\tau_{686}$  is the opacity at 686 GHz, and  $\alpha_{\text{FF},\text{Syn}}$  is the spectral index coming from the free-free/synchrotron emission.

equation (see also Wilson et al. 2014):

$$\frac{S_{\nu_1}}{S_{\nu_2}} = \left( \frac{\nu_1}{\nu_2} \right)^3 \left( \frac{e^{h\nu_2/kT_d} - 1}{e^{h\nu_1/kT_d} - 1} \right) \left( \frac{1 - e^{-\tau_1}}{1 - e^{-\tau_2}} \right) \quad (1)$$

Using the flux densities of the emission at 220 GHz,<sup>9</sup> 350 GHz, and 686 GHz, this allows us to derive the opacities and dust temperatures in the different peaks, as shown in Figure 3 along with the  $\chi^2$  fits. We assumed a spectral index of the dust emissivity<sup>10</sup> of 1.8 (see Wilson et al. 2014 and references therein) and varied the dust temperatures in the range from 2.5 K up to 150 K and opacities at 220 GHz between 0.02 and 1 (corresponding to opacities at 686 GHz of  $\tau_{686} = (\nu_{686}/\nu_{220})^{1.8} \times \tau_{220}$ , i.e.,  $\sim 0.15$ –8). The best-fit solutions suggest dust temperatures of  $\sim 10$ –30 K at low opacities of  $\tau_{686} = 0.19$  for all five peaks, with L2 having the highest  $T_d$  of 25 K. However, L4 and L5 have solutions with almost equally low  $\chi^2$  at higher  $T_d > 60$  K and much higher opacities of  $\tau_{686} = 4$  while the opacities of L2 stay consistently below 1. The two-temperature best-fit ranges are in good agreement with what is found for the molecular gas, which can only be well fit by a gas model with a two-temperature phase (see next sections). As dust and molecular gas are intimately bound, one would expect a two-temperature phase as well in the dust. The higher  $T_d$  values of the inner disk are similar to the values found for the eastern nucleus in Arp 220, which was fitted to  $\sim 80$  K but at higher opacities that are closer to the values found in the western nucleus of Arp 220 (Wilson et al. 2014).

To calculate the dust mass  $M_{\text{dust}}$  at a given frequency for each peak, we use the following standard equation:

$$M_{\text{dust}} = \frac{S_{\nu} D^2}{\kappa_{\nu} B(\nu, T_d)} \quad (2)$$

with  $S_{\nu}$  being the flux observed at frequency  $\nu$ ,  $D$  the distance ( $= 3.5$  Mpc),  $\kappa_{\nu}$  the mass absorption coefficient  $\kappa_{\nu} = \kappa_0(\nu/\nu_0)^{\beta}$  with  $\beta$  being the spectral index of the dust emissivity, and  $B(\nu, T_d)$  the Planck function. Assuming  $\beta = 1.8$  and  $\kappa_{158 \mu\text{m}} \approx 0.6$ – $3 \text{ m}^2 \text{ g}^{-1}$  at a frequency of  $\nu_0 = 1.9$  THz ( $\equiv 158 \mu\text{m}$ ) depending on the dust properties (see Draine & Lee 1984; Zubko et al. 1996, 2004; Dayal et al. 2010; Hirashita et al. 2014), we estimate dust masses of  $\sim 10^4$ – $10^5 M_{\odot}$  per dust peak, i.e., with an uncertainty of a factor of 5–10. The biggest uncertainty comes from the range of  $\kappa_{\nu}$ , which depends on which type or combination of dust grains dominates (i.e., graphite, silicate, amorphous carbon, etc., see Hirashita et al. 2014 for a summary). Comparing the dust masses to the molecular gas masses derived from optically thin molecular tracers (such as  $^{13}\text{CO}$ ) of a few  $\sim 10^7 M_{\odot}$  (see for instance Leroy et al. 2015), we derive a gas-to-dust mass ratio of  $\gtrsim 100$ – $1000$  for the different peaks and the range in  $\kappa$ . Doing the same exercise on the global flux of the entire disk, we find a dust mass of about a few  $10^6 M_{\odot}$  for a dust temperature of  $T_d = 25$  K. The gas mass of the disk in NGC 253 is about a few  $10^8$ – $10^9 M_{\odot}$  in the area of the detected continuum emission, resulting in a global gas-to-dust mass ratio of a few hundred.

<sup>9</sup> Contributions from the free-free/synchrotron emission can be neglected here as they are less than 5%, and hence are smaller than the uncertainties and leave the final best-fit solutions unchanged.

<sup>10</sup> We fitted equally for a spectral indices of 1.5 and 2.1 as used in previous publications for NGC 253 (e.g., Peel et al. 2011), but the best-fit solutions were found for a value of 1.8.

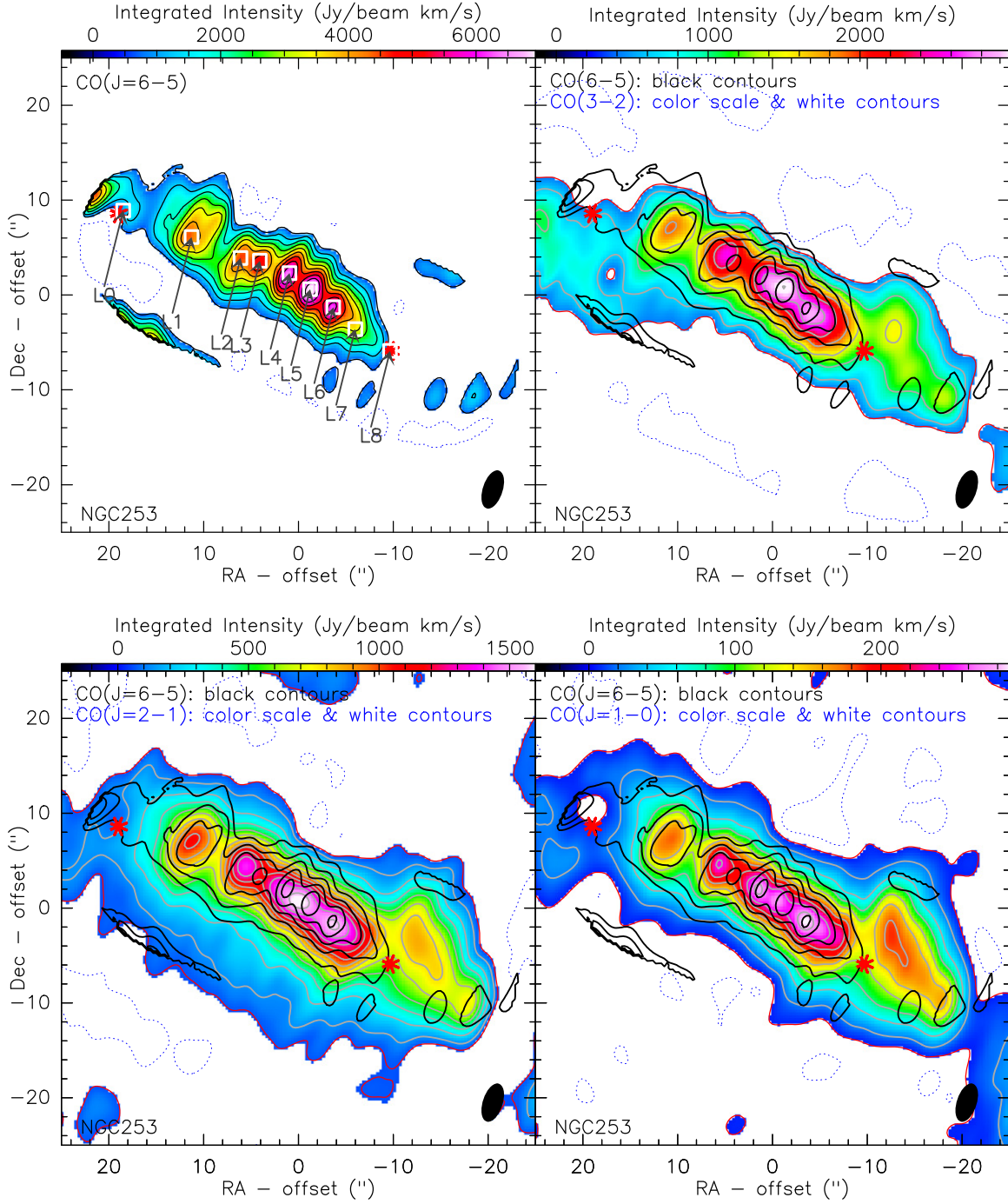


**Figure 4.** Panels comparing the flux distributions of the four  $^{12}\text{CO}$  line transitions. Upper left: the  $^{12}\text{CO}(J = 6-5)$  emission in color scale and contours. Upper right: the  $^{12}\text{CO}(J = 3-2)$  emission (this paper and Sakamoto et al. 2011; in color scale and red and gray contours) overlaid with contours (in black) of the  $^{12}\text{CO}(J = 6-5)$  line emission. Lower left: the same but for the  $^{12}\text{CO}(J = 2-1)$  emission (taken from Sakamoto et al. 2011) overlaid with the contours of the  $^{12}\text{CO}(J = 6-5)$  emission. Lower right: the same but for the  $^{12}\text{CO}(J = 1-0)$  emission (taken from the ALMA science archive) overlaid with the contours of the  $^{12}\text{CO}(J = 6-5)$  emission. The red stars (inner and outer two white squares) mark the positions of the two shells (L0 and L8) from Sakamoto et al. (2006) and L1–L7 (white squares) while the corresponding arrows mark the line peaks of the  $^{12}\text{CO}(J = 6-5)$  emission in order to facilitate the discussion. The contours of the  $^{12}\text{CO}(J = 6-5)$  emission start at  $-3\sigma$ ,  $2\sigma = 660 \text{ Jy km s}^{-1} \text{ beam}^{-1}$  in steps of  $2\sigma$  (upper left panel, otherwise in steps of  $4\sigma$ ). The contours of the  $^{12}\text{CO}(J = 3-2)$  emission start at  $-20\sigma$ ,  $100\sigma = 420 \text{ Jy km s}^{-1} \text{ beam}^{-1}$  in steps of  $100\sigma$ . The contours of the  $^{12}\text{CO}(J = 2-1)$  emission start at  $-50\sigma$ ,  $50\sigma = 64 \text{ Jy km s}^{-1} \text{ beam}^{-1}$  in steps of  $100\sigma$ . The contours of the  $^{12}\text{CO}(J = 1-0)$  emission start at  $-25\sigma$ ,  $25\sigma = 5 \text{ Jy km s}^{-1} \text{ beam}^{-1}$  in steps of  $150\sigma$ .

The gas-to-dust mass ratios are consistent with the values ( $\sim 100$ – $1000$ ) usually found in active galaxies with metallicities around solar (see for instance Rémy-Ruyer et al. 2014).

The global (and individual) dust temperatures found here are in good agreement with previous works on NGC 253 (see for instance Peel et al. 2011). The global dust mass of NGC 253 is similar to that found in nearby active galaxies (see, for instance,

Rémy-Ruyer et al. 2014) but one to two orders of magnitude smaller than that found for nearby (ultra)luminous infrared galaxies (=U)LIRGs such as Arp 220, NGC 6240, or NGC 1614 (see for instance Scoville et al. 2015; Xu et al. 2015). Arp 220 and NGC 6240 show dust masses around a few  $10^9 M_\odot$  and NGC 1614 has a dust mass around  $10^7$ – $10^8 M_\odot$ . This is not surprising because the nuclei in

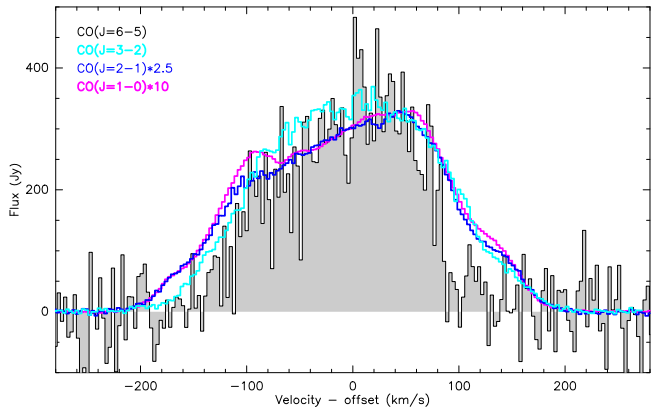


**Figure 5.** The flux of the four different line transitions integrated over the entire emission region for each transition. It is clear from the broad profile that several Gaussian components are present for each CO transition, indicating the presence of multiple molecular clouds or clumps at slightly different velocities. However, the velocity range is similar for each line, indicating that the gas is co-spatial in the clumps.

Arp 220 especially are known to be highly obscured, exhibiting a starburst much stronger than that in the disk of NGC 253, while NGC 1614 is likely more comparable to NGC 253 than Arp 220.

### 3.2. Line Emission

#### 3.2.1. General Properties

We clearly detect emission from  $^{12}\text{CO}(J = 6-5)$  (Figure 4). The distribution of the spectrally integrated  $^{12}\text{CO}(J = 6-5)$  line emission closely follows that of  $^{12}\text{CO}(J = 3-2)$ ,  $^{12}\text{CO}(J = 2-1)$ , and  $^{12}\text{CO}(J = 1-0)$  (see Figure 4). We identify at least seven different peaks in the integrated  $^{12}\text{CO}(J = 6-5)$  emission, labeled L1 to L7 in Figure 4, plus the location of the two shells labeled L0 (for SB2) and L8 (for SB1). L4 to L6 appear to be the most dominant ones in all four  $^{12}\text{CO}$  transitions. L5 is spatially coincident with the dynamical center of NGC 253 (see Müller-Sánchez et al. 2010; Rosenberg et al. 2012). Most of these line peaks in the disk, with the exceptions of L1 and L3 which have no correspondence in the continuum emission, coincide spatially with the continuum peaks at 2.6, 1.3, 0.87, and 0.43 mm identified in Sakamoto et al. (2011) and this work (see also Section 3.1). Line peaks L4 and L5 appear merged for the  $^{12}\text{CO}(J = 3-2)$  and  $^{12}\text{CO}(J = 2-1)$  emission at the angular resolution used in this paper, while they are clearly separated for the  $^{12}\text{CO}(J = 6-5)$  emission. However, at the higher angular resolution used in Sakamoto et al. (2011), the peak positions match well those seen for  $^{12}\text{CO}(J = 6-5)$ , with the exception of L3, which does not have an obvious counterpart in the lower transitions. This merging of the peaks is probably due to extended emission in the lower  $^{12}\text{CO}$  transitions as  $^{12}\text{CO}(J = 6-5)$  most likely traces denser (and/or hotter) gas. L5 appears to be the strongest peak for all lines except  $^{12}\text{CO}(J = 1-0)$ , where L6 seems to dominate. Interestingly, L4 appears to be somewhat brighter in  $^{12}\text{CO}(J = 6-5)$ ,  $^{12}\text{CO}(J = 2-1)$ , and  $^{12}\text{CO}(J = 1-0)$  than in  $^{12}\text{CO}(J = 3-2)$ , an effect that is already seen for the  $^{13}\text{CO}(J = 2-1)$ ,  $\text{C}^{18}\text{O}(J = 2-1)$ , and  $\text{HCN}(J = 4-3)$  emission by Sakamoto et al. (2011).

We detect only marginal  $^{12}\text{CO}(J = 6-5)$  emission around the western and eastern shells (SB1 = L08 and SB2 = L01) described in Sakamoto et al. (2006) and marked with stars

and squares in Figure 4. While the eastern shell is only partially covered with our five-point mosaic of the  $^{12}\text{CO}(J = 6-5)$  emission, the western shell is (almost) completely covered. However, the western shell is already significantly weaker in the lower  $^{12}\text{CO}$  transitions, so that we might still simply lack adequate sensitivity in our observations for a clear detection.

The line profiles of the  $^{12}\text{CO}(J = 6-5)$ ,  $^{12}\text{CO}(J = 3-2)$ ,  $^{12}\text{CO}(J = 2-1)$ , and  $^{12}\text{CO}(J = 1-0)$  emission, shown in Figure 5, were spatially integrated over the entire emission area for each transition. Multiple-component (up to three) Gaussian fits were carried out on the line profiles and the results are given in Table 2. As can be seen, while overall the line profiles agree well with each other, parts of the redshifted and blueshifted wings of the  $^{12}\text{CO}(J = 3-2)$ ,  $^{12}\text{CO}(J = 2-1)$ , and  $^{12}\text{CO}(J = 1-0)$  line emission are apparently missing in the  $^{12}\text{CO}(J = 6-5)$  line emission. These “wing” components are most likely associated with the western (redshifted velocities) and eastern (blueshifted velocities) shells (see Sakamoto et al. 2006). While the eastern part could easily still be hidden in the noise, one gets the impression that the redshifted  $^{12}\text{CO}(J = 6-5)$  emission is indeed not present and that this is more likely due to excitation effects than to insufficient sensitivity as also shown by the individual spectra at the peaks (see Figure 7).

Looking at the velocity channel maps in Figure 6, in which the  $^{12}\text{CO}(J = 6-5)$  emission as an example is plotted in contours over the  $^{12}\text{CO}(J = 1-0)$  emission in color scale, we find again that all four transitions strongly resemble each other for most velocities; notably the three lowest transitions are almost indistinguishable from each other (see also Figures 5 and 7). Although it is difficult to clearly identify the line peaks (Figure 4) of the  $^{12}\text{CO}(J = 6-5)$  emission in the velocity-resolved channels due to the lower signal-to-noise ratios and because each of these peaks represents an ensemble of giant molecular cloud complexes (GMCs), one can still see some trends. L6 clearly is the dominant and brightest peak for the  $^{12}\text{CO}(J = 3-2)$ ,  $^{12}\text{CO}(J = 2-1)$ , and  $^{12}\text{CO}(J = 1-0)$  emission between velocities 24 and  $60 \text{ km s}^{-1}$ , with L4 and L5 being significantly weaker in contrast to the spectrally integrated maps in Figure 4. At these velocities, both L5 and L6 appear almost equally bright in the  $^{12}\text{CO}(J = 6-5)$  emission. L3 and L4 also look equally strong in  $^{12}\text{CO}(J = 6-5)$  for velocities around  $-80$  and  $-48 \text{ km s}^{-1}$ , while L3 seems to be brighter for the lower transitions. The lack of significant  $^{12}\text{CO}(J = 6-5)$  emission at the higher velocities ( $\gtrsim 100 \text{ km s}^{-1}$  and  $\lesssim -100 \text{ km s}^{-1}$ ) with respect to the lower three transitions is again striking.

Figure 7 shows the line spectra taken at the position of each line peak for the four different  $^{12}\text{CO}$  transitions. Again, the similar shapes of the profiles among all four transitions for each peak is striking. This is strong evidence that all four transitions trace the same molecular gas, i.e., the same molecular clumps along the disk of NGC 253. We fitted a multiple-component (up to three) Gaussian to all line profiles. The results of these fits are given in Table 4. To reduce the parameter space for the fit and to remain consistent between the fits for each transition, we fixed the line centers of the three different line components by choosing the best compromise for the line centers between the three lowest transitions after an initial fit to them with the line center as free parameter. In Figure 7 it becomes clear why L6 appears stronger in the velocity channel maps as opposed to L5 in the spectrally integrated map: L5 is weaker but with a

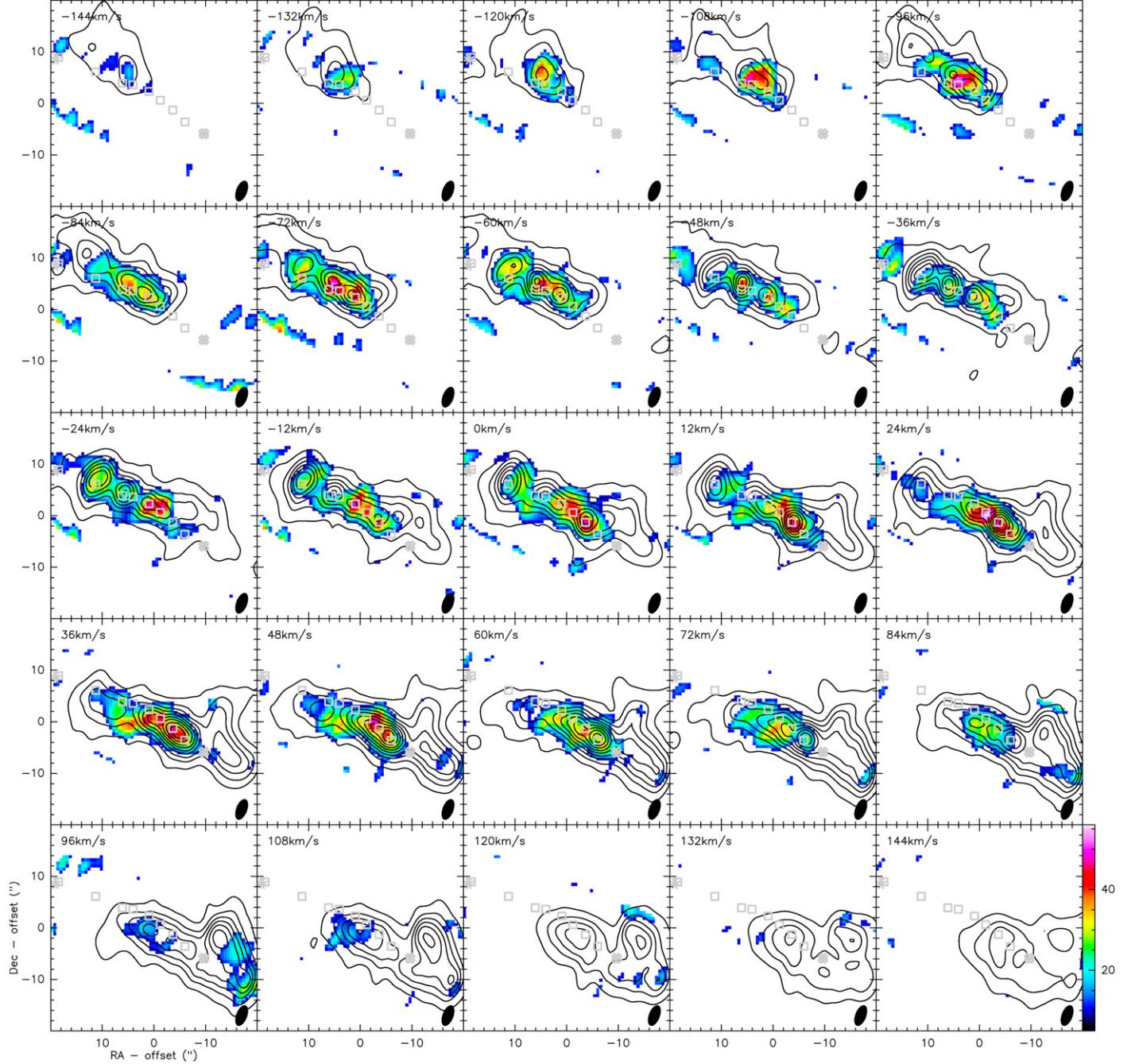


**Figure 6.** Channel maps of the  $^{12}\text{CO}(J = 1-0)$  (black contours) overlaid onto the  $^{12}\text{CO}(J = 6-5)$  emission (color scale). The spectral resolution is  $\sim 12 \text{ km s}^{-1}$ . The contours for the  $^{12}\text{CO}(J = 1-0)$  emission start at  $100\sigma = 0.1 \text{ Jy beam}^{-1} \text{ channel}^{-1}$  and go in steps of  $300\sigma$ . The gray symbols represent the seven different line peaks in the disk and the stars represent the two shells as shown in Figure 4 and specified in Table 4.

much broader line profile than L6. Judging also from these complex line profiles with multiple Gaussian components and given the high inclination of the disk in NGC 253, it is very likely that each of these peaks is an ensemble of GMCs at different velocities and merged along the line of sight. Based on recent ALMA observations of multiple lines in the 3 mm band, Leroy et al. (2015) find in total 10 different cloud components in their data, as based on dense gas tracers such as HCN and HCO, which appear to be fitted as well with up to three Gaussian components similar to our work. Their main components along the disk are in good agreement with those used in this study.

As a note, given the complexity of the peaks, we tried to run a clump finder program on our data cubes (e.g., GAUSSCLUMP from Stutzki & Guesten 1990), but we did not manage to obtain meaningful results due to the added complexity of an (almost) edge-on galaxy for the dynamics as well as the lack of angular resolution. Too many clumps are still merged together in space and velocity so that a clear separation and identification of GMCs remains very difficult at this point.

### 3.2.2. Line Ratios

We calculated the brightness temperature ratios between  $^{12}\text{CO}(J = 6-5)$ ,  $^{12}\text{CO}(J = 3-2)$ ,  $^{12}\text{CO}(J = 2-1)$ , and  $^{12}\text{CO}$

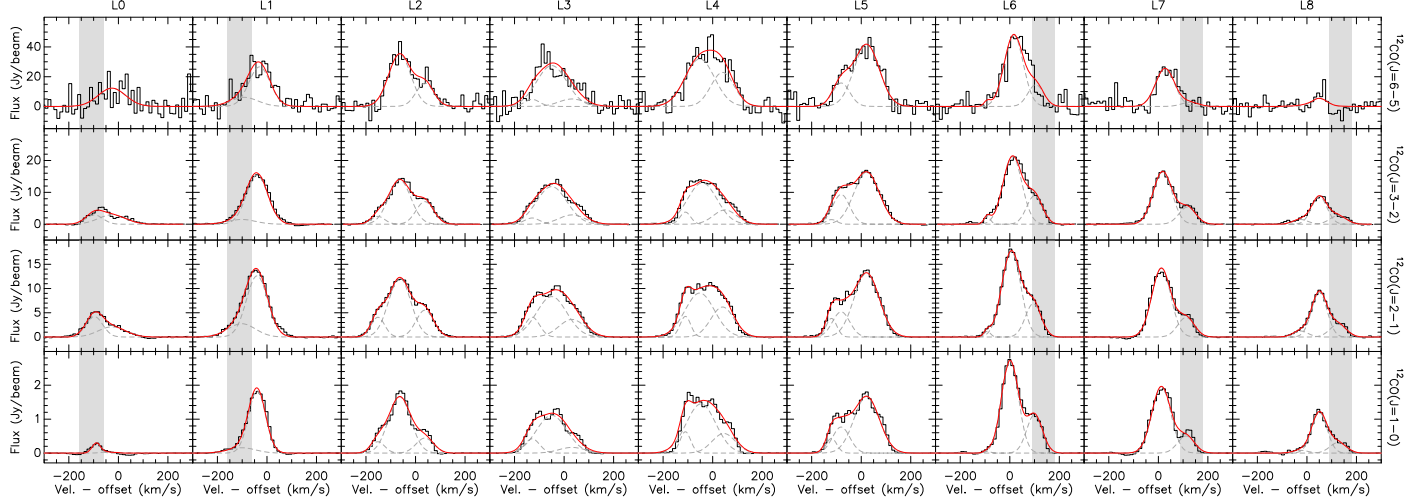


**Figure 7.** Line spectra for the different line peaks for each  $^{12}\text{CO}$  transition. Each row corresponds to one transition (see labeling on the right) and each column to the different line peaks L0 to L8 (see labelling on the top). A Gaussian fit with up to three components has been applied to all spectra, shown as solid red (*sum*) and dashed gray curves (*individual components*). We fixed the velocities and FWHM during the fit to ensure that we fit the same components in all four transitions. The results of these fits are given in Tables 2 and 4. The gray shaded areas approximately mark the velocity ranges for the eastern shell (around L0) and the western shell (around L8 and close to L6/L7) in the wings of the line profiles.

( $J=1-0$ ), using different methods, first converting the intensities from jansky to kelvin. Figure 8 shows the ratios between the spectrally integrated intensity maps from Figure 4, while Table 5 lists the ratios determined from the line profiles shown in Figure 7. We plot the individual line SEDs for each component and Gaussian component in Figure 9. We also compare the line intensities sampled in bins of  $\sim 1''$  and  $12 \text{ km s}^{-1}$  in Figure 10 by using a mask for the different regions (being roughly twice the synthesized beam size); for components L1 to L7 we plot the different velocities in different colors to explore a possible dependence on velocity.

Along the disk, the spectrally integrated ratios (Figure 8) show values of  $R_{32/65}^{\text{CO}} \simeq 1-2$ ,  $R_{21/65}^{\text{CO}} \simeq 2-3$ ,  $R_{10/65}^{\text{CO}} \simeq 0.5-1.5$ ,  $R_{21/32}^{\text{CO}} \simeq 1-1.5$ ,  $R_{10/32}^{\text{CO}} \simeq 0.5-1.5$ , and  $R_{10/21}^{\text{CO}} \simeq 0.3-0.7$ , the range of which is lower than the values determined directly from the line components (Table 5). As Figures 9 and 10 clearly indicate, there are indeed differences between the three different line components for each peak that appear to be identical in the different line transitions. This highlights the fact that at each position we probably see an ensemble of different GMCs that likely exhibit slightly different excitation conditions (see also Table 6). However, the differences are not very large, so probably all of these GMCs are exposed to the same major heating source, the starburst and its winds/shocks.

While we cannot identify any significant difference in the ratios between the peaks along the disk (see also Columns 3–9 in Tables 5 and 6, as well as Figure 9), the temperature ratios are significantly lower close to the eastern shell SB2, indicating much warmer (and/or denser) material there (similar to the continuum emission), and slightly higher toward the western shell SB1, indicating less warm (or less dense) gas there (see Figures 8–10). This difference in gas excitation between the two shells is quite surprising if one assumes a similar nature/origin of the two. However, there are some indications that the two shells are probably caused by different mechanisms: SB2 is

associated with winds from a stellar cluster while SB1 is associated with a supernova remnant.<sup>11</sup> The energetic output of a supernova is probably quite different from the stellar winds from star formation/starbursts in a stellar cluster so that a different feedback to the surrounding molecular gas is to be expected (see also Section 3.2.4). Another explanation could be that these shells are at different evolutionary stages, although they appear to exhibit similar extents and expansion velocities (see Sakamoto et al. 2006; Bolatto et al. 2013) if one believes that SB1 is an expanding superbubble. As Sakamoto et al. (2011) expressed doubts about SB1 being a superbubble as opposed to SB2, SB1 might have a much different origin, thus naturally explaining the different ratios and subsequently the different excitation conditions in these two regions.

However, we have to apply some caution in interpreting these ratios, as we do not have exactly the same uv-coverages in the different  $^{12}\text{CO}$  transitions, with  $^{12}\text{CO}(J=6-5)$  probably being the least well sampled and the least sensitive. We already discussed the effect of spatial filtering flux in a previous section and found that resolution effects are possibly minor along the disk but could be more important in the region of the shells. Therefore, we think that the ratios along the disk are likely very representative while for the shells we probably need more sensitive observations of a larger field with better uv-coverage, as is becoming possible with ALMA.

### 3.2.3. Large Velocity Gradient Analysis

We conducted a large velocity gradient analysis with the RADEX code (see van der Tak et al. 2007), applying a reduced  $\chi^2$  minimization method to fit the basic excitation conditions of the molecular gas in the western and eastern shells and the (averaged) disk. We first considered a one-phase gas model, i.e., gas at one kinetic temperature, one  $\text{H}_2$  density, and one CO column density. We thereby varied the temperatures by  $T_{\text{kin}} = 10-400 \text{ K}$ , the densities by  $n_{\text{H}_2} = 10^3-10^8 \text{ cm}^{-3}$ , and the column densities by  $N_{\text{CO}} = 10^{14}-10^{19} \text{ cm}^{-2}$  for a linewidth of  $dv = 100 \text{ km s}^{-1}$  (see also Leroy et al. 2015) and a uniform sphere, linearly dividing the parameter space into 41 “bins” with steps of 10 K for  $T_{\text{kin}}$  and 0.1 dex for  $n_{\text{H}_2}$  and  $N_{\text{CO}}$ . All

<sup>11</sup> However, one single supernova remnant is probably not enough to create SB1 alone.

**Table 4**  
Molecular Cloud Complexes in all Observed  $^{12}\text{CO}$  Transitions

ID (1)	Bluest Gaussian Line				Central Gaussian Line				Reddest Gaussian Line				
	$S_{1,\nu}^{\text{peak}}$ (2)	$I_{1,\nu}^{\text{peak}}$ (3)	$v_0$ (4)	$\Delta\nu$ (5)	$S_{2,\nu}^{\text{peak}}$ (6)	$I_{2,\nu}^{\text{peak}}$ (7)	$v_0$ (8)	$\Delta\nu$ (9)	$S_{3,\nu}^{\text{peak}}$ (10)	$I_{3,\nu}^{\text{peak}}$ (11)	$v_0$ (12)	$\Delta\nu$ (13)	$\sum_{i=1}^3 (I_{i,\nu}^{\text{peak}})$ (14)
$^{12}\text{CO}(J = 6-5)$													
L0	...	...	...	...	<5.0	<426	-97	80	$12.3 \pm 2.8$	$1699 \pm 406$	-26	130	$1699 \pm 406$
L1	...	...	...	...	$6.1 \pm 2.3$	$846 \pm 324$	-102	130	$26.6 \pm 2.6$	$2860 \pm 398$	-40	101	$3706 \pm 513$
L2	$<5.00$	<346	-152	65	$35.2 \pm 1.8$	$3937 \pm 424$	-64	105	$15.7 \pm 1.9$	$1402 \pm 240$	38	84	$5339 \pm 487$
L3	$<5.00$	<378	-129	71	$27.5 \pm 2.7$	$4218 \pm 511$	-50	144	$5.0 \pm 2.6$	$663 \pm 350$	32	124	$4881 \pm 619$
L4	$<5.00$	<266	-110	50	$32.0 \pm 2.5$	$4767 \pm 509$	-52	140	$22.9 \pm 2.4$	$2684 \pm 376$	40	110	$7451 \pm 633$
L5	$<5.00$	<266	-120	50	$15.8 \pm 2.6$	$1377 \pm 283$	-81	82	$41.7 \pm 1.7$	$5327 \pm 496$	22	120	$6704 \pm 571$
L6	$<5.00$	<160	-91	30	$48.2 \pm 2.4$	$4618 \pm 564$	6	90	$14.6 \pm 2.7$	$1165 \pm 264$	95	75	$5783 \pm 623$
L7	...	...	...	...	$25.6 \pm 2.2$	$2450 \pm 342$	12	90	<5.0	<426	112	80	$2450 \pm 342$
L8	$<5.00$	<378	-26	71	$5.4 \pm 2.0$	$420 \pm 166$	50	73	<5.0	<415	126	78	$420 \pm 166$
$^{12}\text{CO}(J = 3-2)$													
L0	...	...	...	...	$2.9 \pm 0.2$	$249 \pm 37$	-97	80	$3.0 \pm 0.2$	$408 \pm 40$	-26	130	$657 \pm 54$
L1	...	...	...	...	$1.5 \pm 0.2$	$207 \pm 39$	-102	130	$15.4 \pm 0.3$	$1654 \pm 167$	-40	101	$1861 \pm 171$
L2	$2.45 \pm 0.2$	$169 \pm 31$	-152	65	$13.9 \pm 0.2$	$1559 \pm 150$	-64	105	$7.1 \pm 0.2$	$635 \pm 78$	38	84	$2363 \pm 172$
L3	$1.96 \pm 0.4$	$148 \pm 34$	-129	71	$11.8 \pm 0.3$	$1811 \pm 135$	-50	144	$2.9 \pm 0.3$	$386 \pm 51$	32	124	$2345 \pm 148$
L4	$3.81 \pm 0.4$	$203 \pm 47$	-110	50	$13.0 \pm 0.3$	$1938 \pm 145$	-52	140	$4.5 \pm 0.3$	$525 \pm 59$	40	110	$2666 \pm 163$
L5	$1.45 \pm 0.4$	$77 \pm 25$	-120	50	$9.3 \pm 0.3$	$815 \pm 103$	-81	82	$16.4 \pm 0.2$	$2092 \pm 176$	22	120	$2984 \pm 205$
L6	$2.44 \pm 0.6$	$78 \pm 32$	-91	30	$21.3 \pm 0.3$	$2042 \pm 229$	6	90	$8.9 \pm 0.4$	$714 \pm 100$	95	75	$2834 \pm 252$
L7	...	...	...	...	$16.5 \pm 0.2$	$1583 \pm 177$	12	90	$5.4 \pm 0.2$	$457 \pm 59$	112	80	$2040 \pm 187$
L8	$1.50 \pm 0.2$	$113 \pm 20$	-26	71	$8.7 \pm 0.2$	$678 \pm 94$	50	73	$2.7 \pm 0.2$	$222 \pm 31$	126	78	$1013 \pm 101$
$^{12}\text{CO}(J = 2-1)$													
L0	...	...	...	...	$4.2 \pm 0.1$	$360 \pm 46$	-97	80	$2.1 \pm 0.1$	$291 \pm 24$	-26	130	$651 \pm 52$
L1	...	...	...	...	$2.8 \pm 0.1$	$383 \pm 34$	-102	130	$12.6 \pm 0.1$	$1357 \pm 135$	-40	101	$1740 \pm 139$
L2	$4.08 \pm 0.1$	$282 \pm 44$	-152	65	$12.2 \pm 0.1$	$1362 \pm 130$	-64	105	$5.6 \pm 0.1$	$496 \pm 60$	38	84	$2140 \pm 150$
L3	$4.10 \pm 0.2$	$310 \pm 46$	-129	71	$8.3 \pm 0.2$	$1279 \pm 92$	-50	144	$3.6 \pm 0.2$	$479 \pm 44$	32	124	$2068 \pm 112$
L4	$4.27 \pm 0.2$	$227 \pm 47$	-110	50	$9.1 \pm 0.2$	$1353 \pm 99$	-52	140	$6.2 \pm 0.2$	$725 \pm 68$	40	110	$2305 \pm 129$
L5	$3.85 \pm 0.2$	$205 \pm 43$	-120	50	$5.2 \pm 0.2$	$454 \pm 58$	-81	82	$13.2 \pm 0.1$	$1688 \pm 142$	22	120	$2347 \pm 159$
L6	$1.19 \pm 0.1$	$38 \pm 13$	-91	30	$17.7 \pm 0.1$	$1696 \pm 189$	6	90	$6.9 \pm 0.1$	$550 \pm 74$	95	75	$2284 \pm 203$
L7	...	...	...	...	$14.2 \pm 0.2$	$1360 \pm 152$	12	90	$4.0 \pm 0.2$	$344 \pm 45$	112	80	$1704 \pm 159$
L8	$1.25 \pm 0.1$	$95 \pm 15$	-26	71	$9.3 \pm 0.1$	$720 \pm 99$	50	73	$2.6 \pm 0.1$	$219 \pm 29$	126	78	$1034 \pm 104$
$^{12}\text{CO}(J = 1-0)$													
L0	...	...	...	...	$0.30 \pm 0.01$	$25 \pm 3$	-97	80	$0.03 \pm 0.01$	$5 \pm 2$	-26	130	$30 \pm 4$
L1	...	...	...	...	$0.16 \pm 0.02$	$22 \pm 3$	-102	130	$1.84 \pm 0.02$	$197 \pm 20$	-40	101	$219 \pm 20$
L2	$0.34 \pm 0.04$	$23 \pm 4$	-152	65	$1.66 \pm 0.03$	$185 \pm 18$	-64	105	$0.44 \pm 0.03$	$40 \pm 6$	38	84	$248 \pm 19$
L3	$0.42 \pm 0.04$	$32 \pm 5$	-129	71	$1.11 \pm 0.03$	$171 \pm 13$	-50	144	$0.17 \pm 0.03$	$22 \pm 4$	32	124	$225 \pm 14$
L4	$0.63 \pm 0.06$	$34 \pm 8$	-110	50	$1.45 \pm 0.04$	$216 \pm 17$	-52	140	$0.58 \pm 0.04$	$68 \pm 8$	40	110	$318 \pm 20$
L5	$0.43 \pm 0.05$	$23 \pm 5$	-120	50	$0.77 \pm 0.04$	$67 \pm 9$	-81	82	$1.67 \pm 0.03$	$213 \pm 18$	22	120	$303 \pm 21$
L6	$0.06 \pm 0.04$	$2 \pm 1$	-91	30	$2.57 \pm 0.04$	$246 \pm 28$	6	90	$0.95 \pm 0.04$	$76 \pm 11$	95	75	$322 \pm 30$
L7	...	...	...	...	$1.96 \pm 0.03$	$188 \pm 21$	12	90	$0.51 \pm 0.03$	$43 \pm 6$	112	80	$231 \pm 22$
L8	$0.08 \pm 0.01$	$6 \pm 1$	-26	71	$1.20 \pm 0.01$	$93 \pm 13$	50	73	$0.31 \pm 0.01$	$26 \pm 4$	126	78	$125 \pm 14$

**Note.** (1) Names of  $^{12}\text{CO}(J = 6-5)$  line emission peaks as given in this paper (starting with an L). Corresponding  $^{12}\text{CO}(J = 3-2)$  and  $^{12}\text{CO}(J = 2-1)$  names from Sakamoto et al. (2011): L0 = SB2; L2  $\simeq$  Sa1; L4  $\simeq$  Sa2; L5  $\simeq$  Sa3; L6  $\simeq$  Sa4; L7  $\simeq$  Sa5, L8 = SB1. The absolute positions of each of these line peaks are (for  $\alpha = 00^{\circ}47^m$ ,  $\delta = -25^{\circ}17'$ ): L0 =  $34.56^{\circ}$  s,  $09.^{\circ}2$ ; L1 =  $34.07^{\circ}$  s,  $12.^{\circ}0$ ; L2 =  $33.69^{\circ}$  s,  $14.^{\circ}2$ ; L3 =  $33.54^{\circ}$  s,  $14.^{\circ}5$ ; L4 =  $33.31^{\circ}$  s,  $15.^{\circ}8$ ; L5 =  $33.15^{\circ}$  s,  $17.^{\circ}5$ ; L6 =  $32.97^{\circ}$  s,  $19.^{\circ}4$ ; L7 =  $32.80^{\circ}$  s,  $21.^{\circ}7$ ; L8 =  $32.53^{\circ}$  s,  $24.^{\circ}0$ . (2, 3, 6, 7, 10, 11). Peak flux densities  $S_{\nu}$  (in  $\text{Jy beam}^{-1}$ ) and spectrally integrated intensities  $I_{\nu}$  ( $= \int S_{\nu}^{\text{int}} d\nu$  in  $\text{Jy beam}^{-1} \text{ km s}^{-1}$ ) derived at the peak emission for each fitted Gaussian line. (4, 8, 12). Zero velocity is with respect to the redshifted frequency of the observed CO line transition. The central velocities of each Gaussian line component have been first derived by fitting the  $^{12}\text{CO}(J = 2-1)$  and  $^{12}\text{CO}(J = 3-2)$  lines. The values thus found have been averaged and subsequently fixed for each fit. We assume a  $5-10 \text{ km s}^{-1}$  error on the central velocities. The unit is  $\text{km s}^{-1}$ . (5, 9, 13) Full width at half maximum (FWHM) of each line. Identical to the velocity center, the FWHMs have been first derived by fitting the  $^{12}\text{CO}(J = 2-1)$  and  $^{12}\text{CO}(J = 3-2)$  lines, taking the mean of both and subsequently fixing it in the fits for all line transitions. We assume an error on the FWHM of  $5-10 \text{ km s}^{-1}$ . The unit is  $\text{km s}^{-1}$ .

reduced  $\chi_{\text{red}}^2$  results for which the modeled line ratios are within at least  $\sim 1-1.5\sigma$  of the observed line ratios (i.e.,  $\chi_{\text{red}}^2 \leqslant 1.5$ ) were considered as acceptable solutions. With these criteria we could fit the western and eastern shells quite reasonably, while we did not find any solution for the disk that could reproduce the high ratio of  $^{12}\text{CO}(J = 6-5)$  to  $^{12}\text{CO}(J = 1-0)$ . This is in agreement with previous findings on the CO line SED of NGC 253 by different groups based on single-dish and/or satellite (*Herschel*) observations (e.g., Hailey-Dunsheath et al. 2008; Rosenberg et al. 2014). One approach is

to allow for a two-phase gas model by assuming two different kinetic temperatures with an upper limit of the “cold” component at around  $T_{\text{kin,cold}} = 150 \text{ K}$  and  $T_{\text{kin,warm}} > T_{\text{kin,cold}}$ . The range of solutions found for the excitation conditions in the three different regions of NGC 253 is shown in Figure 11. The respective range in kinetic temperatures for the two-component model (middle panel) for a given volume and column density as well as the kinetic temperatures and column densities for the one-component models for a given density (upper and lower panels) are plotted in Figure 12.

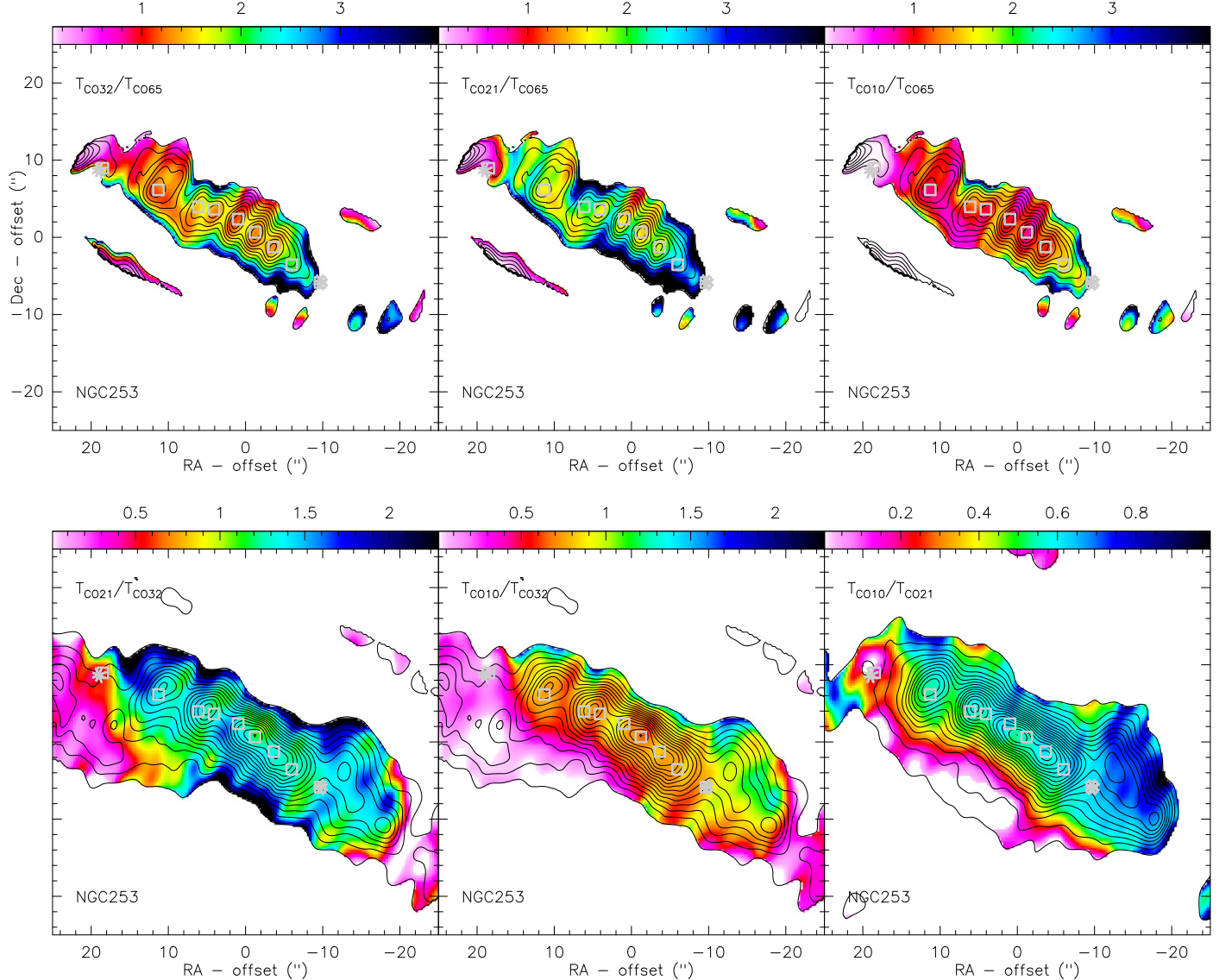


**Figure 8.** Temperature brightness ratios between the different integrated  $^{12}\text{CO}$  line transitions. The gray symbols (squares and stars) are the same as in Figure 4. Contours in the upper panels are those of the  $^{12}\text{CO}(J = 6-5)$  emission while those in the lower panels are from the  $^{12}\text{CO}(J = 1-0)$  line emission. Please note that we used a reversed color scale, i.e., for low ratios bright colors such as white, pink, and red are used while high ratios are represented with darker colors such as blue and black. This was done to facilitate the connection between warm (and/or dense) molecular gas that is reflected here in low line ratios while cooler (and/or less dense) gas is shown by large line ratios.

**Disk:** As just mentioned, a one-temperature phase model largely underestimates the  $^{12}\text{CO}(J = 6-5)$  emission similar to previous findings (e.g., Hailey-Dunsheath et al. 2008; Rosenberg et al. 2014). Our best-fit model suggests a very cold gas component at around 10 K and a very warm one at around 340 K with  $\text{H}_2$  gas densities for both of  $n_{\text{H}_2} = 10^3\text{--}10^4 \text{ cm}^{-3}$  and CO column densities of  $N_{\text{CO}} \simeq 10^{18} \text{ cm}^{-2}$  (see Figure 12). However, as can be seen in Figure 11 and is indicated by the mediocre  $\chi^2$  values in Figure 12, we find a large range of excitation conditions with similarly “good”  $\chi^2$  values as the best-fit model, certainly due to the fact that four observed lines are not sufficient to constrain the parameter space well with four free variables. Furthermore, although the best-fit models fit the observed data reasonably well, the modeled line ratios are only within  $1.5\text{--}2\sigma$  of the observed ones, indicating that a two-temperature phase gas model is still insufficient to reproduce the data and that the assumption of

equal gas and column densities of the two gas phases is too simplistic. However, leaving those as free parameters as well between the two gas phases enforces more observational constraints, i.e., more line transitions and different molecular tracers need to be observed, which is beyond the scope of this paper.

Rosenberg et al. (2014) indeed argue that they need a three-temperature phase gas model to explain their  $^{12}\text{CO}$  ladder, of which the phase-1 low-temperature component is heated through PDRs. The phase-2 and phase-3 components are more likely heated mechanically, while heating through cosmic rays seems to be rather negligible based on their models (see the next Section but also Paglione & Abrahams 2012). The mechanical heating through low-velocity shocks or turbulence is needed to produce the high temperatures throughout the surrounding clouds. PDRs affect only a thin layer of the surrounding molecular clouds and would potentially start to

**Table 5**  
 $^{12}\text{CO}$  Brightness Temperature Ratios from Individual Gaussian Components

Ratio (1)	L0 (2)	L1 (3)	L2 (4)	L3 (5)	L4 (6)	L5 (7)	L6 (8)	L7 (9)	L8 (10)
Bluest Gaussian Line									
$R_{65}^{32}$	...	...	>2.00	>1.60	>3.10	>1.20	>1.90	...	>1.20
$R_{65}^{21}$	...	...	>7.30	>7.40	>7.70	>6.90	>2.10	...	>2.30
$R_{65}^{10}$	...	...	>2.40	>3.00	>4.60	>3.10	>0.4	...	>0.60
$R_{32}^{21}$	...	...	$3.80 \pm 0.90$	$4.70 \pm 1.30$	$2.50 \pm 0.80$	$6.00 \pm 2.30$	$1.10 \pm 0.60$	...	$1.90 \pm 0.40$
$R_{32}^{10}$	...	...	$1.20 \pm 0.30$	$1.90 \pm 0.50$	$1.50 \pm 0.50$	$2.70 \pm 1.10$	$0.20 \pm 0.10$	...	$0.50 \pm 0.10$
$R_{21}^{10}$	...	...	$0.33 \pm 0.08$	$0.41 \pm 0.09$	$0.60 \pm 0.19$	$0.45 \pm 0.14$	$0.21 \pm 0.13$	...	$0.25 \pm 0.06$
$R_{65}^{32}/R_{L4}$	...	...	...	...	...	...	...	...	...
$R_{65}^{21}/R_{L4}$	...	...	...	...	...	...	...	...	...
$R_{65}^{10}/R_{L4}$	...	...	...	...	...	...	...	...	...
$R_{32}^{21}/R_{L4}$	...	...	$1.5 \pm 0.6$	$1.9 \pm 0.8$	1.0	$2.4 \pm 1.2$	$0.4 \pm 0.2$	...	$0.8 \pm 0.3$
$R_{32}^{10}/R_{L4}$	...	...	$0.8 \pm 0.3$	$1.3 \pm 0.6$	1.0	$1.8 \pm 0.9$	$0.2 \pm 0.1$	...	$0.3 \pm 0.1$
$R_{21}^{10}/R_{L4}$	...	...	$0.5 \pm 0.2$	$0.7 \pm 0.3$	1.0	$0.7 \pm 0.3$	$0.4 \pm 0.3$	...	$0.4 \pm 0.2$
Central Gaussian Line									
$R_{65}^{32}$	>2.30	$1.00 \pm 0.40$	$1.60 \pm 0.20$	$1.70 \pm 0.20$	$1.60 \pm 0.20$	$2.40 \pm 0.60$	$1.80 \pm 0.30$	$2.60 \pm 0.50$	$6.50 \pm 2.70$
$R_{65}^{21}$	>7.60	$4.10 \pm 1.60$	$3.10 \pm 0.40$	$2.70 \pm 0.40$	$2.60 \pm 0.30$	$3.00 \pm 0.70$	$3.30 \pm 0.50$	$5.00 \pm 0.90$	$15.40 \pm 6.50$
$R_{65}^{10}$	>2.10	$0.90 \pm 0.40$	$1.70 \pm 0.20$	$1.50 \pm 0.20$	$1.60 \pm 0.20$	$1.80 \pm 0.40$	$1.90 \pm 0.30$	$2.80 \pm 0.50$	$8.00 \pm 3.30$
$R_{32}^{21}$	$3.30 \pm 0.60$	$4.20 \pm 0.90$	$2.00 \pm 0.30$	$1.60 \pm 0.20$	$1.60 \pm 0.20$	$1.30 \pm 0.20$	$1.90 \pm 0.30$	$1.90 \pm 0.30$	$2.40 \pm 0.50$
$R_{32}^{10}$	$0.70 \pm 0.10$	$1.00 \pm 0.20$	$1.10 \pm 0.10$	$0.80 \pm 0.10$	$1.00 \pm 0.10$	$0.70 \pm 0.10$	$1.10 \pm 0.20$	$1.10 \pm 0.20$	$1.20 \pm 0.20$
$R_{21}^{10}$	$0.20 \pm 0.04$	$0.23 \pm 0.04$	$0.54 \pm 0.07$	$0.53 \pm 0.06$	$0.64 \pm 0.07$	$0.59 \pm 0.11$	$0.58 \pm 0.09$	$0.55 \pm 0.09$	$0.52 \pm 0.10$
$R_{65}^{32}/R_{L4}$	>1.4	$0.6 \pm 0.3$	$1.0 \pm 0.2$	$1.1 \pm 0.2$	1.0	$1.5 \pm 0.4$	$1.1 \pm 0.2$	$1.6 \pm 0.4$	$4.0 \pm 1.8$
$R_{65}^{21}/R_{L4}$	>3.0	$1.6 \pm 0.7$	$1.2 \pm 0.2$	$1.1 \pm 0.2$	1.0	$1.2 \pm 0.3$	$1.3 \pm 0.3$	$2.0 \pm 0.4$	$6.0 \pm 2.6$
$R_{65}^{10}/R_{L4}$	>1.3	...	$1.0 \pm 0.2$	$0.9 \pm 0.2$	1.0	$1.1 \pm 0.3$	$1.2 \pm 0.3$	$1.7 \pm 0.4$	$4.9 \pm 2.2$
$R_{32}^{21}/R_{L4}$	$2.1 \pm 0.5$	$2.7 \pm 0.6$	$1.3 \pm 0.2$	$1.0 \pm 0.1$	1.0	$0.8 \pm 0.2$	$1.2 \pm 0.2$	$1.2 \pm 0.2$	$1.5 \pm 0.3$
$R_{32}^{10}/R_{L4}$	$0.6 \pm 0.1$	$1.0 \pm 0.3$	$1.1 \pm 0.2$	$0.8 \pm 0.1$	1.0	$0.7 \pm 0.1$	$1.1 \pm 0.2$	$1.1 \pm 0.2$	$1.2 \pm 0.3$
$R_{21}^{10}/R_{L4}$	$0.3 \pm 0.1$	$0.4 \pm 0.1$	$0.9 \pm 0.2$	$0.8 \pm 0.1$	1.0	$0.9 \pm 0.2$	$0.9 \pm 0.2$	$0.9 \pm 0.2$	$0.8 \pm 0.2$
Reddest Gaussian Line									
$R_{65}^{32}$	$1.00 \pm 0.20$	$2.30 \pm 0.40$	$1.80 \pm 0.40$	$2.30 \pm 1.30$	$0.80 \pm 0.10$	$1.60 \pm 0.20$	$2.50 \pm 0.70$	>4.30	>2.10
$R_{65}^{21}$	$1.50 \pm 0.40$	$4.30 \pm 0.70$	$3.20 \pm 0.70$	$6.50 \pm 3.50$	$2.40 \pm 0.40$	$2.90 \pm 0.40$	$4.20 \pm 1.10$	>7.30	>4.70
$R_{65}^{10}$	$0.11 \pm 0.05$	$2.50 \pm 0.40$	$1.00 \pm 0.20$	$1.20 \pm 0.70$	$0.90 \pm 0.20$	$1.40 \pm 0.20$	$2.30 \pm 0.60$	>3.60	>2.30
$R_{32}^{21}$	$1.60 \pm 0.20$	$1.80 \pm 0.30$	$1.80 \pm 0.30$	$2.80 \pm 0.40$	$3.10 \pm 0.50$	$1.80 \pm 0.20$	$1.70 \pm 0.30$	$1.70 \pm 0.30$	$2.20 \pm 0.40$
$R_{32}^{10}$	$0.11 \pm 0.04$	$1.10 \pm 0.20$	$0.60 \pm 0.10$	$0.50 \pm 0.10$	$1.20 \pm 0.20$	$0.90 \pm 0.10$	$1.00 \pm 0.20$	$0.80 \pm 0.20$	$1.10 \pm 0.20$
$R_{21}^{10}$	$0.07 \pm 0.03$	$0.58 \pm 0.08$	$0.32 \pm 0.06$	$0.18 \pm 0.04$	$0.38 \pm 0.06$	$0.50 \pm 0.06$	$0.55 \pm 0.11$	$0.50 \pm 0.10$	$0.47 \pm 0.10$
$R_{65}^{32}/R_{L4}$	$1.2 \pm 0.40$	$3.0 \pm 0.7$	$2.3 \pm 0.6$	$3.0 \pm 1.7$	1.0	$2.0 \pm 0.4$	$3.1 \pm 1.0$	>5.5	>2.7
$R_{65}^{21}/R_{L4}$	$0.6 \pm 0.20$	$1.8 \pm 0.4$	$1.3 \pm 0.3$	$2.7 \pm 1.5$	1.0	$1.2 \pm 0.3$	$1.7 \pm 0.5$	>3.0	>2.0
$R_{65}^{10}/R_{L4}$	$0.1 \pm 0.05$	$2.7 \pm 0.7$	$1.1 \pm 0.3$	$1.3 \pm 0.8$	1.0	$1.6 \pm 0.4$	$2.6 \pm 0.8$	>4.0	>2.5
$R_{32}^{21}/R_{L4}$	$0.5 \pm 0.10$	$0.6 \pm 0.1$	$0.6 \pm 0.1$	$0.9 \pm 0.2$	1.0	$0.6 \pm 0.1$	$0.6 \pm 0.1$	$0.5 \pm 0.1$	$0.7 \pm 0.2$
$R_{32}^{10}/R_{L4}$	$0.1 \pm 0.04$	$0.9 \pm 0.2$	$0.5 \pm 0.1$	$0.4 \pm 0.1$	1.0	$0.8 \pm 0.2$	$0.8 \pm 0.2$	$0.7 \pm 0.2$	$0.9 \pm 0.2$
$R_{21}^{10}/R_{L4}$	$0.2 \pm 0.09$	$1.5 \pm 0.3$	$0.9 \pm 0.2$	$0.5 \pm 0.1$	1.0	$1.3 \pm 0.2$	$1.5 \pm 0.4$	$1.3 \pm 0.3$	$1.3 \pm 0.3$

**Note.** (1–10) First six rows: brightness temperature ratios between the different  $^{12}\text{CO}$  transitions derived for each line peak (Table 2). We converted all  $^{12}\text{CO}$  integrated peak intensities from jansky to kelvin. Rows 7–12: brightness temperature ratios with respect to peak L4.

dissociate the CO molecules due to the strong UV-radiation fields (see also Kaufmann & Neufeld 1996; Goicoechea et al. 2013; Rosenberg et al. 2014).

**Western Shell (L8):** Our best-fit solutions suggest two main scenarios for the western shell due to the  $T_{\text{kin}}\text{--}n_{\text{H}_2}$  degeneracy of  $^{12}\text{CO}$  in the excitation: the molecular gas is either (1) at rather high kinetic temperatures around 300 K but low H<sub>2</sub> gas densities around  $\sim 10^3 \text{ cm}^{-3}$ , or (2) at lower kinetic temperatures around 60 K but high H<sub>2</sub> gas densities around  $\sim 5 \times 10^3 \text{ cm}^{-3}$  (see Figures 11 and 12). Only in the case of low  $T_{\text{kin}}$  and high  $n(\text{H}_2)$  can the CO column density be well constrained and show values of about  $\sim 10^{18} \text{ cm}^{-2}$ , similar to the disk and the eastern shell (see Figure 12), while the case of high  $T_{\text{kin}}$  and low  $n(\text{H}_2)$  leaves open almost the entire range of column densities sampled here. The HCN emission has been

found to be stronger (by a factor of  $\sim 3$  in integrated fluxes) in the western shell than in the eastern shell by Leroy et al. (2015). This is likely incompatible with the case in which the gas in the western shell is significantly less dense than in the eastern shell, hence favoring the case of low  $T_{\text{kin}}$  and high  $n(\text{H}_2)$ . The kinetic temperature of 60 K in this case is in between the cold ( $T_{\text{kin}} \approx 10$  K) and hot ( $T_{\text{kin}} \approx 340$  K) gas components found for the disk but much lower than found for the eastern shell (see next paragraph).

**Eastern Shell (L0):** The best-fit solution for the eastern shell suggests higher kinetic temperatures ( $T_{\text{kin}} = 360$  K) than the disk and the western shell but at similar H<sub>2</sub> densities ( $n_{\text{H}_2} \approx 5 \times 10^3 \text{ cm}^{-3}$ ) and CO column densities ( $N_{\text{CO}} \approx 10^{18} \text{ cm}^{-2}$ ). However, it seems that the best-fit model slightly underestimates the  $^{12}\text{CO}(J=2\text{--}1)$  emission as indicated by the

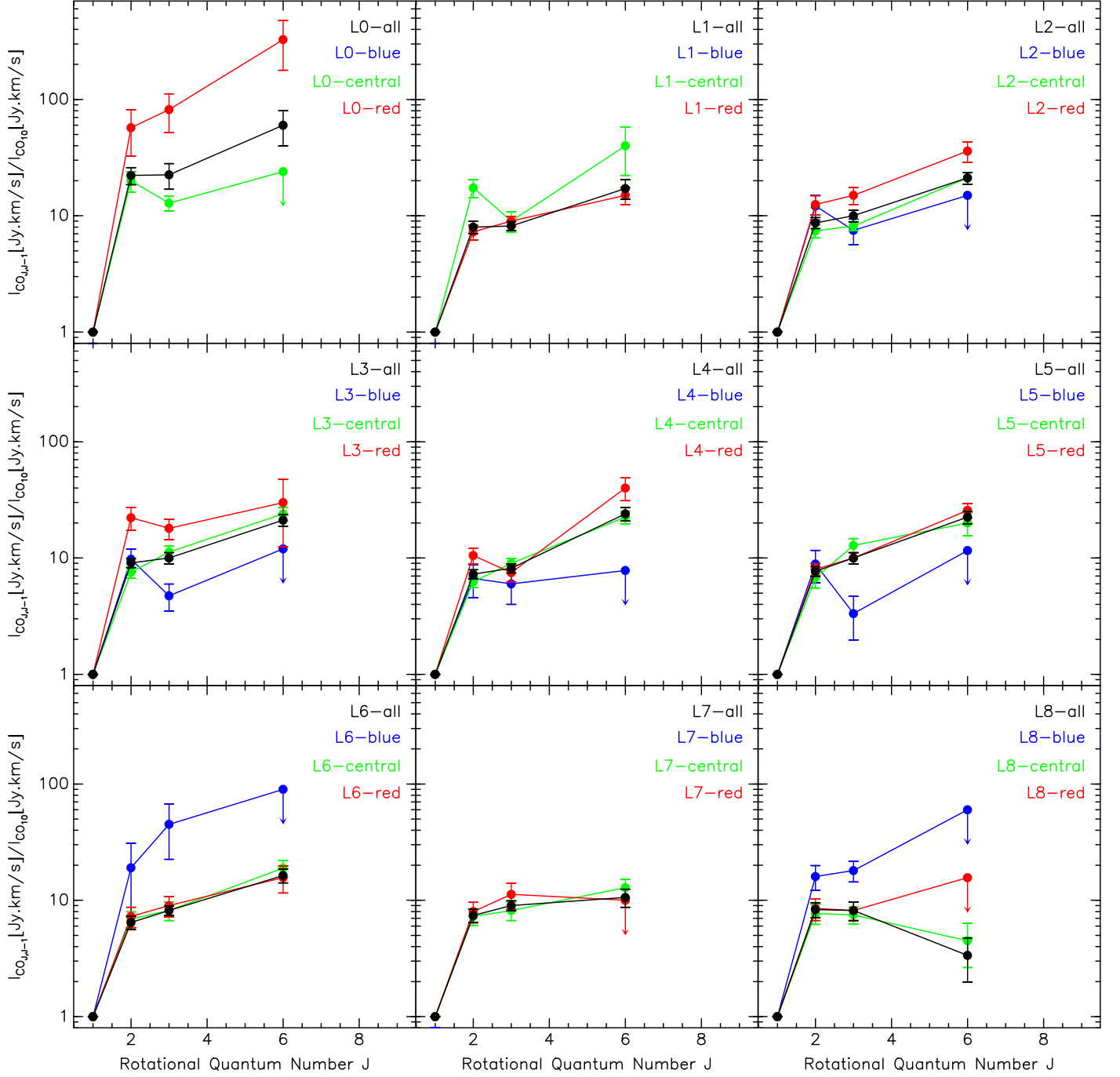


**Figure 9.** CO line SEDs for each position (L0–L9) and Gaussian components (in black (*sum*), blue (*blueshifted* velocities), green (*central* velocities), and red (*redshifted* velocities)). The line intensities, from which the line ratios were derived and plotted here, were not converted into temperature scale ( $\text{K km s}^{-1}$ ) first, as opposed to Tables 5 and 6, in order to remain consistent with CO line SEDs from other publications (e.g., Papadopoulos et al. 2010).

lowest  $\chi^2_{\text{red}}$  of  $\sim 1.2$ , which means that not all modeled line ratios lie within  $1\sigma$  of the observed ones. We also ran a two-temperature phase gas model for the eastern shell similar to the disk but we did not find a solution in which the  $^{12}\text{CO}(J=2-1)$  emission was correctly reproduced. The best-fit solutions of the two-temperature phase models largely resembled the one-temperature phase models, so we decided to keep the one-temperature phase model for the eastern shell for reasons of simplicity. Either we are seeing (part of) the warm component from the disk only here or additional excitation mechanisms have to be considered.

### 3.2.4. Comparison to Other Multi-transition CO Studies

Studies of spatially resolved, multi-transition ( $\geq 4$ )  $^{12}\text{CO}$  emission in galaxies are still very rare. Most of them are conducted with single-dish telescopes that provide sufficient angular resolution to resolve GMC scales ( $\leq 50\text{--}100$  pc) only in the most nearby galaxies or our own galaxy, if at all. We picked several  $^{12}\text{CO}$  ladder studies in order to compare them with the results obtained on NGC 253 (Emprechtinger et al. 2009; Carilli et al. 2010; Riechers et al. 2010; van der Werf et al. 2010; Danielson et al. 2011; Goicoechea et al. 2013; Meijerink et al. 2013; Topal et al. 2014). The studied objects

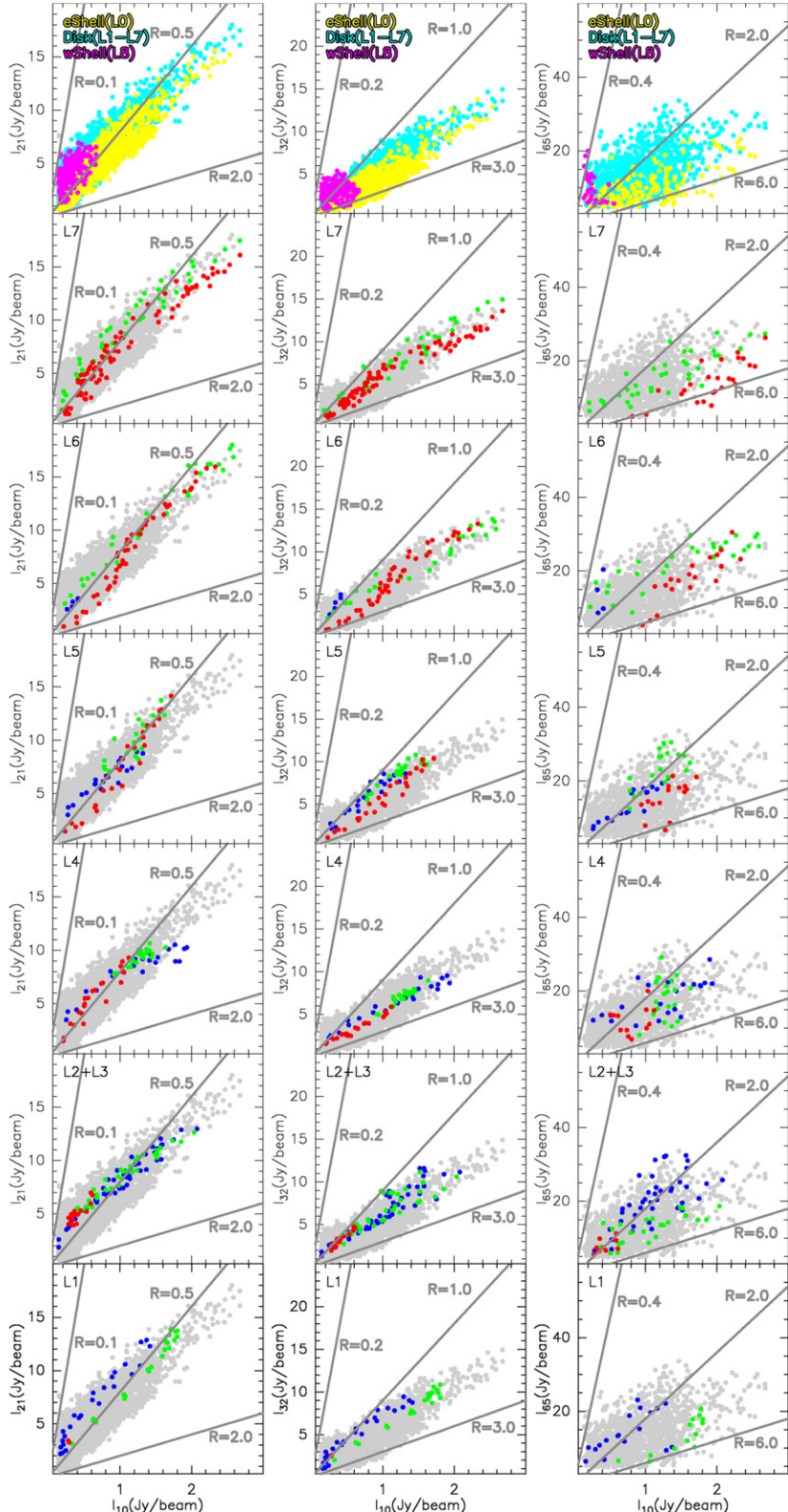


**Figure 10.** Comparison of  $^{12}\text{CO}$  line fluxes for the different line transitions (left column:  $^{12}\text{CO}(J = 2 - 1)$  vs.  $^{12}\text{CO}(J = 1 - 0)$ , middle column:  $^{12}\text{CO}(J = 3 - 2)$  vs.  $^{12}\text{CO}(J = 1 - 0)$ , right column:  $^{12}\text{CO}(J = 6 - 5)$  vs.  $^{12}\text{CO}(J = 1 - 0)$ ) and regions in NGC 253 (L1–L8; from bottom to top) derived from data cubes with matching spatial and spectral resolution ( $4.\prime\prime2 \times 2.\prime\prime1$  and  $12 \text{ km s}^{-1}$ ; we defined a region of  $\sim 8''$  (i.e., twice the synthesized beam) around each line peak defined in Figure 4). We used a sampling spacing of  $\sim 4$  pixels per beam. We only plot points that are above  $3\sigma$  for  $^{12}\text{CO}(J = 6 - 5)$  and  $10\sigma$  for the rest (due to the limited dynamical range). The blue-, red-, and green-colored points represent the blueshifted ( $< -40 \text{ km s}^{-1}$ ; in blue) and redshifted velocities ( $> +40 \text{ km s}^{-1}$ ; in red) and around the systemic velocity of NGC 253 (i.e., from  $-40 \text{ km s}^{-1}$  to  $+40 \text{ km s}^{-1}$ ; in green), respectively. The gray data points are all data points, i.e., from all velocities and all regions.  $R$  represent the brightness temperature ratio and is defined as  $R = T_{\text{CO}10}/T_{\text{CO},J-1}$  for  $J = 6, 3, 2$ . The solid lines are meant to guide the eyes for a given fixed ratio.

**Table 6**  
 $^{12}\text{CO}$  Brightness Temperature Ratios Derived from the Sum of Individual Gaussian Components

Ratio (1)	L0 (2)	L1 (3)	L2 (4)	L3 (5)	L4 (6)	L5 (7)	L6 (8)	L7 (9)	L8 (10)
$R_{65}^{32}$	$1.50 \pm 0.40$	$2.00 \pm 0.30$	$1.80 \pm 0.20$	$1.90 \pm 0.30$	$1.40 \pm 0.10$	$1.80 \pm 0.20$	$2.00 \pm 0.30$	$3.30 \pm 0.60$	$9.60 \pm 3.90$
$R_{65}^{21}$	$3.40 \pm 0.90$	$4.20 \pm 0.70$	$3.60 \pm 0.40$	$3.80 \pm 0.50$	$2.80 \pm 0.30$	$3.10 \pm 0.30$	$3.60 \pm 0.50$	$6.30 \pm 1.10$	$22.10 \pm 9.00$
$R_{65}^{10}$	$0.60 \pm 0.20$	$2.10 \pm 0.40$	$1.70 \pm 0.20$	$1.70 \pm 0.20$	$1.50 \pm 0.20$	$1.60 \pm 0.20$	$2.20 \pm 0.30$	$3.40 \pm 0.60$	$10.70 \pm 4.40$
$R_{32}^{21}$	$2.20 \pm 0.30$	$2.10 \pm 0.30$	$2.00 \pm 0.20$	$2.00 \pm 0.20$	$1.90 \pm 0.20$	$1.80 \pm 0.20$	$1.80 \pm 0.20$	$1.90 \pm 0.20$	$2.30 \pm 0.30$
$R_{32}^{10}$	$0.40 \pm 0.10$	$1.10 \pm 0.10$	$0.90 \pm 0.10$	$0.90 \pm 0.10$	$1.10 \pm 0.10$	$0.90 \pm 0.10$	$1.10 \pm 0.10$	$1.00 \pm 0.10$	$1.10 \pm 0.20$
$R_{21}^{10}$	$0.18 \pm 0.03$	$0.50 \pm 0.06$	$0.46 \pm 0.05$	$0.44 \pm 0.04$	$0.55 \pm 0.05$	$0.52 \pm 0.05$	$0.62 \pm 0.08$	$0.54 \pm 0.07$	$0.48 \pm 0.07$
$R_{65}^{32}/R_{L4}$	$1.1 \pm 0.3$	$1.4 \pm 0.3$	$1.2 \pm 0.2$	$1.3 \pm 0.2$	$1.0$	$1.2 \pm 0.2$	$1.4 \pm 0.2$	$2.3 \pm 0.5$	$6.7 \pm 2.8$
$R_{65}^{21}/R_{L4}$	$1.2 \pm 0.3$	$1.5 \pm 0.3$	$1.3 \pm 0.2$	$1.4 \pm 0.2$	$1.0$	$1.1 \pm 0.2$	$1.3 \pm 0.2$	$2.2 \pm 0.4$	$8.0 \pm 3.4$
$R_{65}^{10}/R_{L4}$	$0.4 \pm 0.1$	$1.4 \pm 0.3$	$1.1 \pm 0.2$	$1.1 \pm 0.2$	$1.0$	$1.1 \pm 0.2$	$1.4 \pm 0.2$	$2.2 \pm 0.4$	$7.0 \pm 3.0$
$R_{32}^{21}/R_{L4}$	$1.1 \pm 0.2$	$1.1 \pm 0.2$	$1.0 \pm 0.1$	$1.0 \pm 0.1$	$1.0$	$0.9 \pm 0.1$	$0.9 \pm 0.1$	$1.0 \pm 0.2$	$1.2 \pm 0.2$
$R_{32}^{10}/R_{L4}$	$0.4 \pm 0.1$	$1.0 \pm 0.2$	$0.9 \pm 0.1$	$0.8 \pm 0.1$	$1.0$	$0.9 \pm 0.1$	$1.0 \pm 0.2$	$0.9 \pm 0.1$	$1.0 \pm 0.2$
$R_{21}^{10}/R_{L4}$	$0.3 \pm 0.1$	$0.9 \pm 0.1$	$0.8 \pm 0.1$	$0.8 \pm 0.1$	$1.0$	$0.9 \pm 0.1$	$1.1 \pm 0.2$	$1.0 \pm 0.2$	$0.9 \pm 0.2$

**Notes.** (1–10) First six rows: brightness temperature ratios between the different  $^{12}\text{CO}$  transitions derived from the sum of all line peaks (Table 2). We converted all  $^{12}\text{CO}$  integrated peak intensities from jansky to kelvin. Rows 7–12: brightness temperature ratios with respect to peak L4.

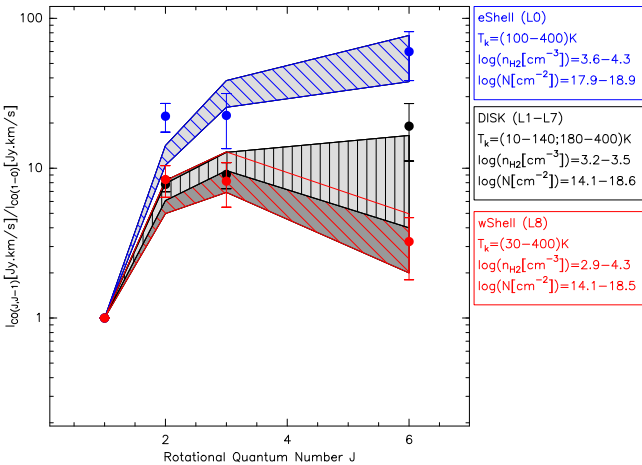


**Figure 11.** CO line SEDs for the eastern shell (blue filled circles), western shell (red filled circles), and central disk (black filled circles), summing up all Gaussian components. The hashed gray areas indicate the range of solutions with equally low  $\chi^2$  fits (i.e., solutions that are within  $\sim 1\text{--}2\sigma$  of the observed values) from RADEX simulations of the line ratios (here derived from the intensities in  $\text{Jy km s}^{-1}$ , as opposed to Table 6 where they were derived from temperatures). The best-fit solution intervals are given in the small colored boxes to the right.

range from GMCs in the Galactic center, over nearby starburst and/or AGN galaxies such as NGC 6946, M82, and NGC 1068, to ULIRGs like Arp 220 and Mrk 231, and high-redshift galaxies.

**Disk:** Interestingly, all studies, i.e., for all (active) environments in our vicinity up to the high-redshift universe, seem to need a multi-phase gas model (with at least higher and lower temperature gas components) to be able to reproduce the observed multi-transition CO emission (e.g., Weiß et al. 2005; Emprechtinger et al. 2009; Carilli et al. 2010; Riechers et al. 2010; van der Werf et al. 2010; Danielson et al. 2011; Goicoechea et al. 2013; Topal et al. 2014), similar to the central disk in NGC 253. Also, most of them find that, besides photoelectric heating from UV radiation in PDRs, mechanical heating through low-velocity shocks has also to be considered as an almost equally dominant mechanism to heat the molecular gas (see also García-Burillo et al. 2010, 2014; Krips

et al. 2011). In all these regions, cosmic rays do not seem to contribute significantly to the heating of the warm molecular gas component, agreeing with the findings by Rosenberg et al. (2014) (see also Meijerink et al. 2011). On the other hand, NGC 253 has known supernova explosions at a rate of  $<0.2 \text{ yr}^{-1}$  (see Paglione & Abrahams 2012; Rampadarath et al. 2014) and, more importantly, a median cosmic-ray ionization rate of  $\zeta_{\text{CR}} \approx 6 \times 10^{-12} \text{ s}^{-1}$  (Paglione & Abrahams 2012). This is a factor of  $\sim 100\text{--}1000$  higher than found in the vicinity of Sgr A\* (Goto et al. 2008) and of the order of the X-ray/(cosmic-ray) ionization rates of  $>10^{-13} \text{ s}^{-1}$  found in the (U)LIRGs Arp 220 and NGC 4418 (González-Alfonso et al. 2013). Goicoechea et al. (2013) mention that already a cosmic-ray ionization rate of  $\zeta_{\text{CR}} \approx 10^{-14} \text{ s}^{-1}$  can heat the gas up to  $\gg 10 \text{ K}$  and Paglione & Abrahams (2012) conclude that “cosmic ray penetration and heating is an important contributor to the warm temperatures observed in starburst galaxies.” Although the simulations conducted by Rosenberg et al. (2014) favor a minor role of cosmic-ray heating, it probably cannot be completely excluded at this point. Moreover, in the case of the ULIRG Mrk 231, van der Werf et al. (2010) find indications that, besides PDR heating, X-ray/(cosmic-ray) heating is a significant contributor in order to explain their two-temperature phase model of the multi-transition CO emission, although they do not include shock models in their simulations. On the other hand, Rangwala et al. (2011) find in the case of Arp 220 that mechanical heating should be largely dominating over that from PDRs, X-ray dissociation regions (XDRs), and cosmic rays, at least for the warm molecular gas. This result might be logical as Arp 220 is a known major merger in an evolved merging stage so that mechanical heating should be quite significant. Although NGC 6240 is in a slightly earlier merger stage than Arp 220, Meijerink et al. (2013) argue for a (low-velocity, C-type) shock domination of the gas heating there as well, similar to Arp 220.

In contrast to NGC 1068, whose molecular gas in its central  $\sim 200 \text{ pc}$  disk is most likely dominated by a combination of (low-velocity) shocks and a giant XDR (e.g., Krips et al. 2011; García-Burillo et al. 2014; Viti et al. 2014), the line transition ratios in NGC 253 decrease (for  $\text{CO}(J_{\text{upper}}-J_{\text{lower}})/\text{CO}(J=1-0)$ ; with  $J_{\text{upper}} > 1$ ) while those for NGC 1068 increase. This is in good agreement with theoretical predictions of the  $^{12}\text{CO}$

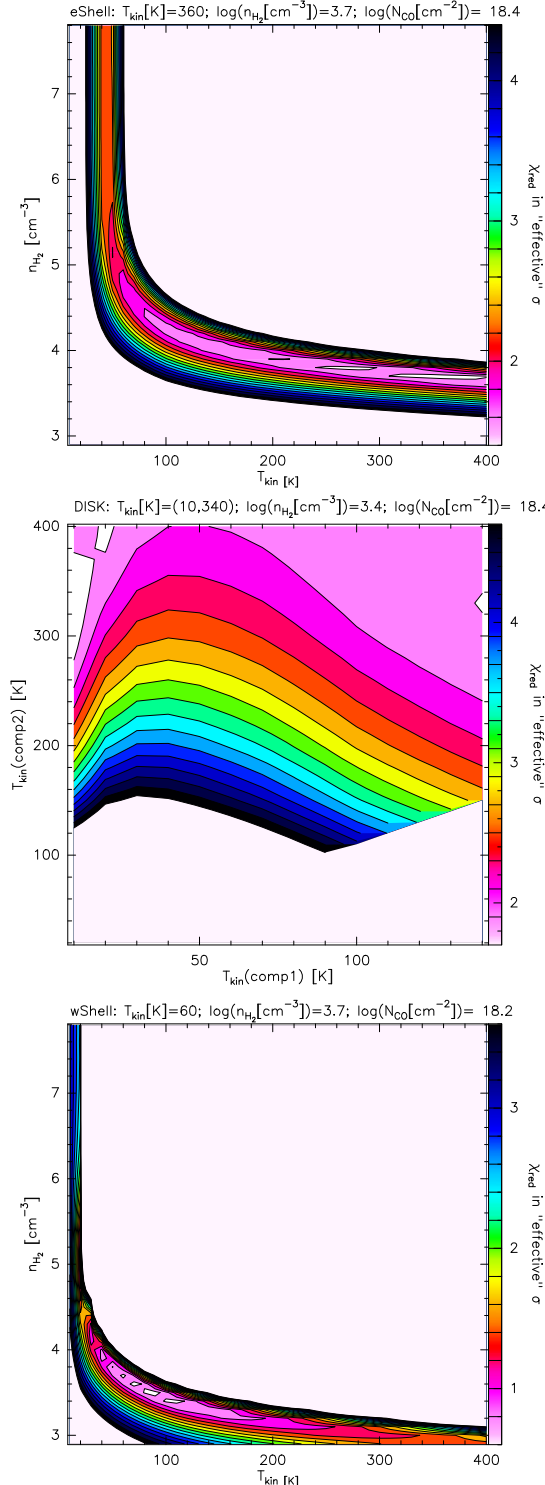


**Figure 12.** Best-fit solutions with the lowest  $\chi_{\text{red}}$  for the three different regions. For the one-phase gas models of the western shell (wShell/L8, upper panel) and eastern shell (eShell/L0, lower panel) we plot the kinetic temperatures and CO column densities as function of  $\chi_{\text{red}}^2$  for a given  $\text{H}_2$  density while for the two-phase gas model we show the two kinetic temperatures for a given  $\text{H}_2$  density and CO column density (given as ( $T_{\text{kin}}(\text{comp1})$ ,  $T_{\text{kin}}(\text{comp2})$ ) above the middle panel with  $T_{\text{kin}}(\text{comp1})$  for the “cold” and  $T_{\text{kin}}(\text{comp2})$  for the warm gas phase). The reduced  $\chi_{\text{red}}$  can be seen as effective  $\sigma$ s, meaning that a  $\chi_{\text{red}}$  of 1 (2,...) represents modeled line ratios that are on average within  $1\sigma$  ( $2\sigma$ ,... ) of the respective observed line ratios. The solutions with the absolute lowest  $\chi_{\text{red}}$  are given above each panel, but note the range of possible solutions with equally low  $\chi_{\text{red}}$  (these ranges are given in Figure 11). The regions in pale pink have  $\chi_{\text{red}}$  outside the range shown in the wedges and have hence been “blanked.”

line ratios for XDRs and PDRs (Meijerink et al. 2006), even in the case of a strong cosmic-ray ionization field in addition to a PDR. Another interesting difference to note is that NGC 1068 indeed shows variations of its line ratios as one gets closer to the nucleus (central 50 pc or so), as revealed by recent ALMA observations (see García-Burillo et al. 2014; Viti et al. 2014), while the disk (central 500 pc) appears to be dominated by the same heating source. Hence, a starburst influences its surrounding gas on a much larger scale than an AGN seems to do.

**Shells:** Based on the discussion of the heating mechanisms responsible for the CO ladder in diverse environments, one can draw some first conclusions on the dominant heating mechanisms for the two shells by simple comparison. As mentioned before, probably only mechanical energy from shocks or turbulent gas can heat up the bulk of molecular gas significantly above 50 K, while photoelectric (PDR) and/or cosmic-ray heating dominates the cold to warm gas component. Our data quite clearly indicate that the eastern shell is much warmer than the disk and the western shell while being at similar gas and column densities. This could hence be an indication that shocks might play a much more dominant role in the eastern shell, associated with a compact stellar cluster, than in the PDR+shock-dominated disk and the western shell, which might be connected to a supernova remnant. It appears rather unlikely that a strong PDR (or cosmic rays) also has to be considered for the eastern shell, which could explain the stronger emission in the higher- $J$  transitions in it compared to the disk; the higher- $J$  CO transitions are more dominantly excited than the lower- $J$  CO transitions.

Our data suggest that the western shell is much colder than the eastern shell and the hot gas component of the disk but is still warmer than its cold gas component. One conclusion, although certainly quite speculative at this point, is that the cosmic rays from the supernova remnant dominate the gas excitation in the western shell and that the (low-velocity) shocks, if they exist, from the supernova (SN) explosion have not yet or only very inefficiently heated the gas to the same high temperatures as found in the (warm component of the) disk or the eastern shell. However, given the similar extent of both shells, it is not intuitive why shocks play such a minor role in the western shell compared to the eastern shell and the disk. Also, while it is true that SNe have been identified through radio observations in the western shell, the lack of radio detections in the eastern shell does not exclude SNe in it. Further observations of either  $^{12}\text{CO}$  or other shock and cosmic-ray tracers have to be conducted to unveil the heating mechanisms in these shells at a sufficient confidence level.

#### 4. SUMMARY

We have presented new interferometric observations of the extended  $^{12}\text{CO}(J = 6-5)$  line and 686 GHz continuum emission in NGC 253 carried out as a five-point mosaic with the SMA. These data were then compared to three lower- $J$   $^{12}\text{CO}$  transitions ( $J = 1-0$ ,  $J = 2-1$ ,  $J = 3-2$ ) and continuum emission at lower frequencies at a similar angular resolution of  $\sim 4''$  observed with ALMA and the SMA.

Five of the eight  $^{12}\text{CO}$  line peaks find counterparts in the millimeter and submillimeter continuum emission, underlining the thermal nature of the continuum emission from dust as suggested by the spectral index of 3 determined from the

different frequencies. The continuum emission at the lowest frequency of 115 GHz appears to exhibit already a significant contribution from non-thermal synchrotron and thermal free-free processes (between 15%–80%) as supported by the spectral indices derived at centimeter wavelengths. We derive dust temperatures of  $\sim$ 10–25 K for the different continuum peaks in the disk with low opacities of  $\sim$ 0.2 at 686 GHz. However, we also find indications for a hotter dust component at least in the inner disk of NGC 253 with dust temperatures exceeding 60 K and at much larger opacities of around 4 at 686 GHz. The latter dust component approaches the values found for ULIRGs such as Arp 220. We estimate a total dust mass of a few  $10^6 M_{\odot}$  for the entire disk, splitting up into  $\sim$ 10 $^4$ –10 $^5 M_{\odot}$  for the GMCs at the individual continuum peaks. Based on the gas masses of each of the peaks, we find a gas-to-dust mass ratio of the order of  $\sim$ 100–1000.

The  $^{12}\text{CO}(J=6-5)$  emission follows nicely the distribution of the molecular gas seen in the lower- $J$  transitions with roughly eight peaks along the disk. Little  $^{12}\text{CO}(J=6-5)$  emission is detected close to the two shells emerging from the edges of the central disk. While the  $^{12}\text{CO}$  line transition ratios do not vary significantly along the disk, the two shells show quite different ratios not only compared to the disk but also compared to each other. The line ratios found along the disk seem to necessitate a two-phase gas model in agreement with previous studies on NGC 253 as well as multiple  $^{12}\text{CO}$  observations on other active galaxies. This two-phase gas model is mainly based on two temperatures, a cool gas component at around  $T_{\text{kin}} = 10$  K and a hot gas component at around  $T_{\text{kin}} = 300$  K. Following a similar line of argument to previous publications, the lower temperature gas is probably dominated by the PDR while the higher temperature gas is a consequence of the shocks found throughout the disk (see also Rosenberg et al. 2012, 2014). However, a possible contribution from cosmic rays, given the high cosmic-ray ionization rate within the disk, cannot be completely excluded for either temperature phase at this point although some simulations indicate only a minor role for cosmic-ray heating (e.g., Rosenberg et al. 2014). While the eastern shell exhibits even warmer gas ( $T_{\text{kin}} > 300$  K) than the hot gas component ( $T_{\text{kin}} \simeq 300$  K) of the disk, the western shell contains gas much cooler ( $T_{\text{kin}} \simeq 60$  K) than the eastern shell but at a temperature somewhere in between those of the two gas components of the disk ( $T_{\text{kin}}^{\text{cold}} \simeq 10$  K and  $T_{\text{kin}}^{\text{hot}} \simeq 300$  K); the gas densities ( $n(\text{H}_2) \simeq 5 \times 10^3 \text{ cm}^{-3}$ ) and column densities ( $N(\text{CO}) \simeq 10^{18} \text{ cm}^{-2}$ ) are very similar in the two shells and the disk. This reflects either a different evolutionary stage of the shells, an additional, different or more efficient heating mechanism in the eastern shell, a very different nature of these two structures, or a combination thereof. However, follow-up observations are essential to put our findings for the shells onto a more solid basis.

The Submillimeter Array is a joint project between the Smithsonian Astrophysical Observatory and the Academia Sinica Institute of Astronomy and Astrophysics and is funded by the Smithsonian Institution and the Academia Sinica. This paper makes use of the following ALMA data: ADS/JAO.ALMA#2011.0.00172.S. ALMA is a partnership of ESO (representing its member states), NSF (USA), and NINS (Japan), together with NRC (Canada) and NSC and ASIAA (Taiwan), in cooperation with the Republic of Chile. The Joint

ALMA Observatory is operated by ESO, AUI/NRAO, and NAOJ. K.S. was supported by the grant NSC 102-2119-M-001-001-MY3. The National Radio Astronomy Observatory is a facility of the National Science Foundation operated under cooperative agreement by Associated Universities Inc. We thank the anonymous referee for thorough and constructive comments.

*Facilities:* SMA, ALMA.

## REFERENCES

- Aladro, R., Martín, S., Martín-Pintado, J., et al. 2011, *A&A*, **535**, 84  
 Bayet, E., Gerin, M., Phillips, T. G., & Contursi, A. 2004, *A&A*, **427**, 45  
 Bendo, G. J., Beswick, R. J., D'Cruze, M. J., et al. 2015, *MNRAS*, **450**, 80  
 Beuther, H., Zhang, Q., Reid, M. J., et al. 2006, *ApJ*, **636**, 323  
 Bolatto, A., Warren, S. R., Leroy, A. K., et al. 2013, *Natur*, **499**, 450  
 Bradford, C. M., Nikola, T., Stacey, G. J., et al. 2003, *ApJ*, **586**, 891  
 Carilli, C. L., Daddi, E., Riechers, D., et al. 2010, *ApJ*, **714**, 1407  
 Carilli, C. L., Kohno, K., Kawabe, R., et al. 2002, *AJ*, **123**, 1838  
 Danielson, A. L. R., Swinbank, A. M., Smail, Ian, et al. 2011, *MNRAS*, **410**, 1687  
 Dayal, P., Hirashita, H., & Ferrara, A. 2010, *MNRAS*, **403**, 620  
 Draine, B. T., & Lee, H. M. 1984, *ApJ*, **285**, 89D  
 Emprechtinger, M., Wiedner, M. C., Simon, R., et al. 2009, *A&A*, **496**, 731  
 Fabbiano, G., & Trinchieri, G. 1984, *ApJ*, **286**, 491  
 García-Burillo, S., Combes, F., Usero, A., et al. 2014, *A&A*, **567**, A125  
 García-Burillo, S., Martín-Pintado, J., Fuente, A., & Neri, R. 2000, *A&A*, **355**, 499  
 García-Burillo, S., Usero, A., Fuente, A., et al. 2010, *A&A*, **519**, 2  
 Goicoechea, J. R., Etxaluze, M., Cernicharo, J., et al. 2013, *ApJL*, **769**, L13  
 González-Alfonso, E., Fischer, J., Bruderer, S., et al. 2013, *A&A*, **550**, 25  
 Goto, M., Usuda, T., Nagata, T., et al. 2008, *ApJ*, **688**, 306  
 Hailey-Dunsheath, S., Nikola, T., Stacey, G. J., et al. 2008, *ApJL*, **689**, L109  
 Heckman, T. M., Armus, L., & Miley, G. K. 1990, *ApJS*, **74**, 833  
 Heesen, V., Beck, R., Krause, M., & Dettmar, R.-J. 2011, *A&A*, **535**, 79  
 Hirashita, H., Ferrara, A., Dayal, P., & Ouchi, M. 2014, *MNRAS*, **443**, 1704  
 Houghton, S., Whiteoak, J. B., Koribalski, B., et al. 1997, *A&A*, **325**, 923  
 Kaufmann, M. J., & Neufeld, D. A. 1996, *ApJ*, **456**, 611  
 Knudsen, K. K., Walter, F., Weiss, A., et al. 2007, *ApJ*, **666**, 156  
 Koribalski, B. S., Staveley-Smith, L., Kilborn, V. A., et al. 2004, *AJ*, **128**, 16  
 Krips, M., Martín, S., Eckart, A., et al. 2011, *ApJ*, **736**, 37  
 Krips, M., Neri, R., García-Burillo, S., et al. 2008, *ApJ*, **677**, 262  
 Leroy, A. K., Walter, F., Decarli, R., et al. 2015, *ApJ*, **801**, 25  
 Martín, S., Martín-Pintado, J., & Viti, S. 2009, *ApJ*, **706**, 1323  
 Martín, S., Mauersberger, R., Martín-Pintado, J., Henkel, C., & García-Burillo, S. 2006, *ApJS*, **164**, 450  
 Matsushita, S., Iono, D., Petitpas, G. R., et al. 2009, *ApJ*, **693**, 56  
 Meier, D. S. 2015, *ApJ*, **801**, 63  
 Meijerink, R., Kristensen, L. E., Weiß, A., et al. 2013, *ApJL*, **762**, L16  
 Meijerink, R., Spaans, M., Loenen, A. F., & van der Werf, P. P. 2011, *A&A*, **525**, 119  
 Meijerink, R., Spaans, M., & Israel, F. P. 2006, *ApJL*, **650**, L103  
 Minh, Y. C., Muller, S., Liu, S.-Y., & Yoon, T. S. 2007, *ApJL*, **661**, L135  
 Mouhcine, M., Ferguson, H. C., Rich, R. M., Brown, T. M., & Smith, T. E. 2005, *ApJ*, **633**, 810  
 Müller-Sánchez, F., González-Martín, O., Fernández-Ontiveros, J. A., Acosta-Pulido, J. A., & Prieto, M. A. 2010, *ApJ*, **716**, 1166  
 Nakashima, J.-I., Fong, D., Hasegawa, T., et al. 2007, *AJ*, **134**, 2035  
 Ott, J., Weiss, A., Henkel, C., & Walter, F. 2005, *ApJ*, **629**, 767  
 Paglione, T. A. D., & Abrahams, R. D. 2012, *ApJ*, **755**, 106  
 Papadopoulos, P. P., Isaak, K. G., & van der Werf, P. P. 2007, *ApJ*, **668**, 815  
 Papadopoulos, P. P., van der Werf, P., Isaak, K., & Xilouris, E. M. 2010, *ApJ*, **715**, 775  
 Peel, M. W., Dickinson, C., Davies, R. D., Clements, D. L., & Beswick, R. J. 2011, *MNRAS*, **416**, 99  
 Qi, C., Wilner, D. J., & Calvet, N. 2006, *ApJL*, **636**, L157  
 Rampadarath, H., Morgan, J. S., Lenc, E., & Tingay, S. J. 2014, *AJ*, **147**, 5  
 Rangwala, N., Maloney, P.R., Glenn, J., et al. 2011, *ApJ*, **743**, 94  
 Rekola, R., Richer, M. G., McCall, M. L., et al. 2005, *MNRAS*, **361**, 330  
 Rémy-Ruyer, A., Madden, S. C., Galliano, F., et al. 2014, *A&A*, **563**, 31  
 Riechers, D., Capak, P. L., Carilli, C. L., et al. 2010, *ApJL*, **729**, L131  
 Roloffs, R., Schilke, P., Zhang, Q., & Zapata, L. 2011, *A&A*, **536**, 33

- Rosenberg, M. J. F., Kazandjian, M. V., van der Werf, P. P., et al. 2014, *A&A*, **564**, 126
- Rosenberg, M. J. F., van der Werf, P. P., & Israel, F. P. 2013, *A&A*, **550**, 12
- Sakamoto, K., Ho, P. T. P., Iono, D., et al. 2006, *ApJ*, **636**, 685
- Sakamoto, K., Mao, R.-Q., Matsushita, S., et al. 2011, *ApJ*, **735**, 19
- Scoville, N., Sheth, K., Walter, F., et al. 2015, *ApJ*, **800**, 70
- Sliwa, K., Wilson, Ch. D., Krips, M., et al. 2013, *ApJ*, **777**, 126
- Stutzki, J., & Guesten, R. 1990, *ApJ*, **356**, 513
- Telesco, C. M., & Harper, D. A. 1980, *ApJ*, **235**, 392
- Topal, S., Bayet, E., Bureau, M., Davis, T. A., & Walsh, W. 2014, *MNRAS*, **437**, 1434
- Ulvestad, J. S., & Antonucci, R. R. J. 1997, *ApJ*, **488**, 621
- van der Tak, F. F. S., Black, J. H., Schöier, F. L., Jansen, D. J., & van Dishoeck, E. F. 2007, *A&A*, **468**, 627
- van der Werf, P. P., Isaak, K. G., Meijerink, R., et al. 2010, *A&A*, **518**, L42
- Viti, S., García-Burillo, S., Fuente, A., et al. 2014, *A&A*, **570**, 28
- Weiß, A., Walter, F., & Scoville, N. Z. 2005, *A&A*, **438**, 533
- Wilson, C. D., Rangwala, N., Glenn, J., et al. 2014, *ApJL*, **789**, L36
- Xu, C. K., Cao, C., Lu, N., et al. 2014, *ApJ*, **787**, 48
- Xu, C. K., Cao, C., Lu, N., et al. 2015, *ApJ*, **799**, 11
- Zapata, L. A., Loinard, L., Rodríguez, L. F., et al. 2013, *ApJL*, **764**, L14
- Zubko, V., Dwek, E., & Arendt, R. G. 2004, *ApJS*, **152**, 211
- Zubko, V. G., Mennella, V., Colangeli, L., & Bussoletti, E. 1996, *MNRAS*, **282**, 1321